Materials Horizons

ROYAL SOCIETY OF CHEMISTRY

REVIEW

View Article Online
View Journal | View Issue

Cite this: *Mater. Horiz.*, 2022, **9**, 194

Printing fabrication of large-area non-fullerene organic solar cells

Peiyao Xue,[a] Pei Cheng,[b] Ray P. S. Han*[a] and Xiaowei Zhan*[a]

Received 16th August 2021,
Accepted 29th September 2021

DOI: 10.1039/d1mh01317c

rsc.li/materials-horizons

Organic solar cells (OSCs) based on a bulk heterojunction structure exhibit inherent advantages, such as low cost, light weight, mechanical flexibility, and easy processing, and they are emerging as a potential renewable energy technology. However, most studies are focused on lab-scale, small-area (<1 cm^2) devices. Large-area (>1 cm^2) OSCs still exhibit considerable efficiency loss during upscaling from small-area to large-area, which is a big challenge. In recent years, along with the rapid development of high-performance non-fullerene acceptors, many researchers have focused on developing large-area non-fullerene-based devices and modules. There are three essential issues in upscaling OSCs from small-area to large-area: fabrication technology, equipment development, and device component processing strategy. In this review, the challenges and solutions in fabricating high-performance large-area OSCs are discussed in terms of the abovementioned three aspects. In addition, the recent progress of large-area OSCs based on non-fullerene electron acceptors is summarized.

1. Introduction

Solar cells are an attractive technology to harvest inexhaustible renewable clean energy from the sun. Organic solar cells (OSCs), as a next-generation photovoltaic technology alternative to traditional silicon-based ones, possess several advantages, such as low cost, light weight, mechanical flexibility and short energy payback time.[1,2] The first OSC was invented in 1958, in which magnesium phthalocyanine was the single-component active layer, and yielded a very low open-circuit voltage (V_{OC}) of only 0.2 V.[3] In 1986, Tang[4] invented a bilayer OSC, in which the donor (copper phthalocyanine) and the acceptor (a perylene tetracarboxylic derivative) were separately vacuum-deposited. The bulk heterojunction structure was invented in the 1990s,[5–7] which developed into one of the most efficient device structures in organic solar cells. A sufficient donor/acceptor interface along with an ideal bicontinuous interpenetrating network is beneficial for exciton dissociation and charge transport.

[a] *Key Laboratory of Polymer Chemistry and Physics of Ministry of Education, School of Materials Science and Engineering, Peking University, Beijing, 100871, P. R. China. E-mail: ray-han@pku.edu.cn, xwzhan@pku.edu.cn*
[b] *College of Polymer Science and Engineering, Sichuan University, Chengdu, 610065, P. R. China*

Peiyao Xue

Peiyao Xue received her BS degree in materials science and engineering from Tianjin University in 2017. Now she is a PhD student in Peking University. Her research interests focus on the fabrication of organic solar cells.

Pei Cheng

Pei Cheng received his BE in Polymer Materials and Engineering from Sichuan University in 2011. He then joined Prof. Xiaowei Zhan's group at the Institute of Chemistry, Chinese Academy of Sciences (ICCAS)/Peking University, and received his PhD in Chemistry (2016). Dr Cheng worked in Prof. Yang Yang's group in the Department of Materials Science and Engineering at the University of California, Los Angeles from 2017 to 2020 as a Postdoc Researcher. He is currently a professor at Sichuan University. His research interests are focused on organic solar cells.

Fullerene acceptors such as $PC_{61}BM$ (phenyl-C_{61}-butyric acid methyl ester) and $PC_{71}BM$ (phenyl-C_{71}-butyric acid methyl ester) have dominated the OSC field over 20 years, since they have some unique advantages, such as high electron affinity and isotropic electron-transporting ability with high electron mobility, which are beneficial for charge separation and charge transport. However, their weak light absorption in the visible and near-infrared (NIR) regions, morphological instability and large energy loss limited further development of the OSC field.[8] The maximum theoretical power conversion efficiency (PCE) of fullerene-based OSCs is ~13%.[9] In 2015, the Zhan group invented a high-performance non-fullerene acceptor, the star molecule ITIC,[10] then pioneered the concept of "fused-ring electron acceptors" (FREAs).[11–13] FREAs generally consist of an electron-donating fused-ring core, electron-accepting end groups, π-bridges and side chains. Molecular structure modularity benefits chemical tailoring and property modulation. The strong intramolecular charge transfer between the fused-ring core and terminal groups enhances light absorption, especially in the 700–1000 nm region. The planar and rigid molecular backbone reduces energy disorder and reorganization energy and facilitates charge transport. Out-of-plane side chains effectively adjust the molecular packing and prevent excessive aggregation, which is beneficial for suitable phase separation and morphological stability. As a result, FREA-based OSCs show low voltage loss, high efficiency and good stability.[12] Up until now, thousands of FREAs have been synthesized,[14–21] and the champion PCEs of FREA-based OSCs exceed 18%.[22–24] Except for high PCE values, the unique optical and electrical properties of FREAs endow them with great application potential. FREAs show strong NIR absorption, which is suitable for fabricating rear active layers of tandem devices[25–28] and semi-transparent or even fully transparent devices suitable for implementation in buildings and windows or greenhouse agrivoltaics.[29–37] FREAs have long exciton diffusion lengths and high electron mobilities, which are beneficial for fabricating thick-film and large-area devices.[38–40] Furthermore, FREAs can also be used in photodetectors[41] and other electronic devices, exhibiting great application potentials.[12]

Some groups focused on developing large-area scalable OSCs. In 2009, Krebs *et al.*[42] reported fully roll-to-roll (R2R) processed OSCs with an inverted architecture of polyethylene terephthalate (PET)/indium tin oxide (ITO)/zinc oxide (ZnO)/photoactive layer/poly(3,4-ethylenedioxythiophene):poly(styrenesulfonate) (PEDOT:PSS)/silver (Ag), which is referred to as "ProcessOne". ProcessOne mainly contains five steps, including etching pretreatment, slot-die coating of the ZnO layer, active layer and PEDOT:PSS layer and screen printing of the silver electrode. Many reported large-scale OSC devices and modules are based on this R2R process.[43,44]

Compared with small-area OSCs, large-area OSCs still exhibit relatively lower PCE values. Most large-area OSCs are based on fullerene acceptors, which have been summarized in some reviews.[45–54] In recent years, along with the rapid development of high-performance non-fullerene acceptors, more research groups started to fabricate large-area devices and modules based on emerging non-fullerene acceptors.[55] Since non-fullerene acceptors exhibit different packing and aggregation behaviors compared with fullerene acceptors, new methods for the construction of high-performance non-fullerene-based large-area OSCs are highly desired. In this review, we discussed the challenges and solutions in fabricating high-performance large-area OSCs in terms of three aspects: fabrication technology, equipment development and device component processing strategy. In addition, we summarized the progress of printed OSCs based on non-fullerene electron acceptors, especially FREAs.

2. Large-area fabrication technologies: printing and coating

Large-area OSCs are generally fabricated by addition-, subtraction-, and pattern-based manufacturing technologies. The widely used methods, including printing, coating and vacuum evaporation, belong to addition-based technology, where additional components are added onto the substrates and basic substrates have not been damaged. Laser ablation

Ray P. S. Han

Ray P. S. Han received his PhD from the University of British Columbia. He is a professor of materials science and engineering at Peking University. His research is focused on flexible electrodes for flexible Li-ion batteries and supercapacitors, harvesting ambient nano–mesoscale energy for self-powered sensors and devices, and nano–microfluidic devices.

Xiaowei Zhan

Xiaowei Zhan received his PhD in polymer chemistry from Zhejiang University in 1998. He was then a postdoctoral researcher and an associate professor at ICCAS from 1998 to 2002. Dr Zhan worked at the University of Arizona and Georgia Institute of Technology from 2002 to 2006 as a research associate/scientist. He has been a full professor at ICCAS since 2006 and joined Peking University in 2012. His research interests are in the development of materials for organic electronics and photonics.

and photolithography belong to subtraction-based technology, where partial materials are removed from the substrates, and are usually used in large-area module fabrication. The third one is pattern-based technology, including wetting/de-wetting, imprinting or bonding methods.

Among the addition-based manufacturing technologies, solution processing (printing/coating) is the most convenient. Printing (including screen printing, gravure printing, flexographic printing, pad printing, offset printing and so on) is a stamping process, where a complex two-dimensional (2D) pattern can be formed. Comparatively, coating is a simple and direct film-forming technology, where a simple zero-dimensional or one-dimensional pattern can be formed. Coating technologies mainly include casting, spin coating, spray coating, doctor blade coating, slot-die coating, knife-over-edge coating, and floating film transfer methods. Inkjet printing is a coating technology but is capable of producing complex 2D patterns.

2.1 Single-substrate fabrication

For single-substrate fabrication, the active layer is printed or coated onto an isolated rigid/flexible substrate. According to the principle of transferring materials onto the substrate, the printing and coating technologies can be classified into of non-contact and contact.

2.1.1 Non-contact fabrication. Casting is one of the simplest film-forming technologies (Fig. 1a); the ink is poured onto the substrate, and no further post-processing or complex facilities are needed. Although it is possible to produce thick films, it is difficult to accurately control the film thickness and uniformity at the whole film scale. Coffee ring effects are observed at the edge of the film owing to the inhomogeneous surface tension of pouring ink.[56,57] Meanwhile, particle aggregation and precipitation occur during the film drying process if material solubility is limited.

Spin coating is a contact/non-contact fabrication technology (Fig. 1b); a certain amount of ink is dropped onto the substrate, followed by spinning the substrate at a certain speed. Alternatively, the liquid solution can be dropped while the substrate is spinning. During the spinning, most of the solution is ejected or volatilized, and only a thin film remains on the substrate. Film thickness and surface/bulk morphology are highly related to spinning speed, ink concentration, ink viscosity and ink volatility. The film thickness can be expressed by the empirical relationship:

$$d = k\omega^{\alpha}, \quad (1)$$

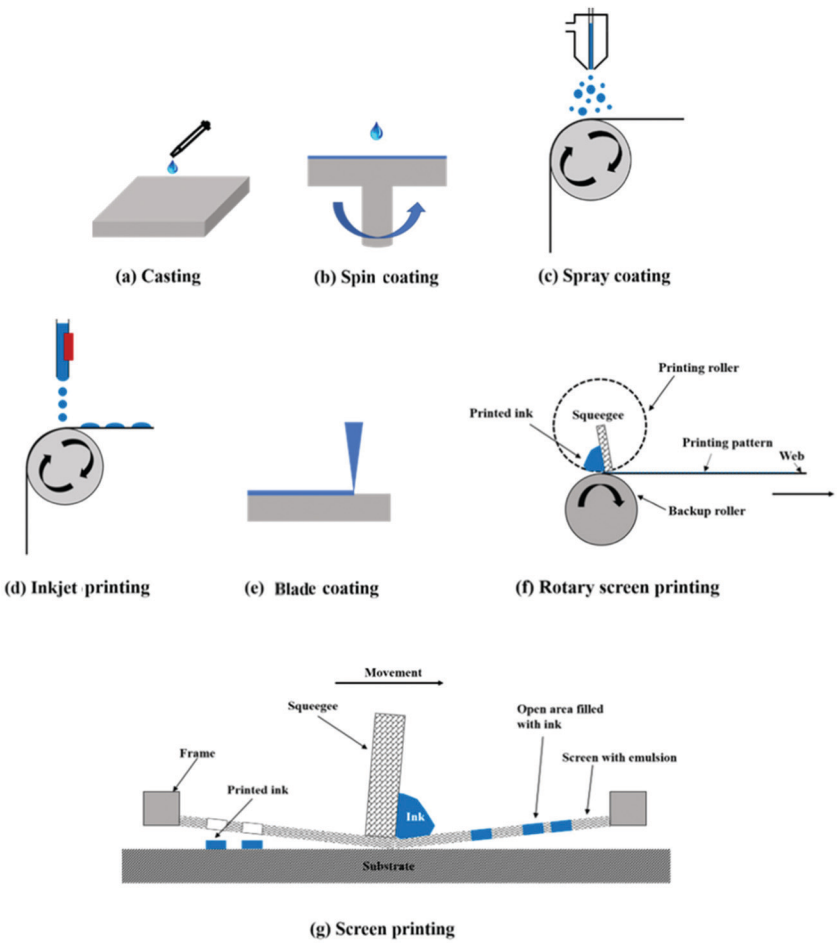

Fig. 1 Single substrate-based fabrication technologies. Reproduced with permission.[47] Copyright 2020, the authors, under the Creative Commons Attribution 3.0 license (c and d). Reproduced with permission.[45] Copyright 2009, Elsevier (f and g).

where ω is the angular velocity, k and α are empirical constants, related to solvent properties, and d is the film thickness.[45] Spin coating is the most important and widely used technology in small-area solution-processed OSCs. The film thickness and morphology of spin-coated films are highly reproducible with the same solvent, solution concentration, and spinning speed. However, it is controversial whether it is suitable for upscaling production. Firstly, the large amount of wasted solution is not suitable for large-scale fabrication; secondly, spin coating is incompatible with continuous production, which is necessary for large-scale production; thirdly, patterning is difficult to be realized, which impedes the module fabrication.

Spray coating is a non-contact, R2R compatible fabrication technology (Fig. 1c); the ink is sprayed through a nozzle and a fine aerosol is formed.[58,59] Generally, spray coating is composed of four steps:[60] liquid atomization,[61] in-flight droplet evaporation,[62] drop impact on the surface[63] and droplet drying. This kind of technology exhibits good ink generality with a wide range of viscosity and volatility of spraying ink. In order to direct the aerosol to the expected location to form patterns, a carrier gas and a pair of electrostatic charging parallel plates are often adopted. The drawback of spray coating is the uncontrollable film smoothness. To form a uniform film, the aerosol droplets have to spread uniformly upon reaching the substrate, which is difficult to be guaranteed. As a result, this method is not frequently used in practical R2R fabrication.

Inkjet printing is a non-contact and high-material-utilization fabrication technology, beneficial for printing various functional layers (Fig. 1d). It involves two steps, ejecting inks from the nozzle to form droplets and forming precise patterns on the target substrate under control.[64–67] According to different droplet generation principles, inkjet printing is divided into continuous inkjet printing (CIP) and drop-on-demand (DoD) inkjet printing (Fig. 2).

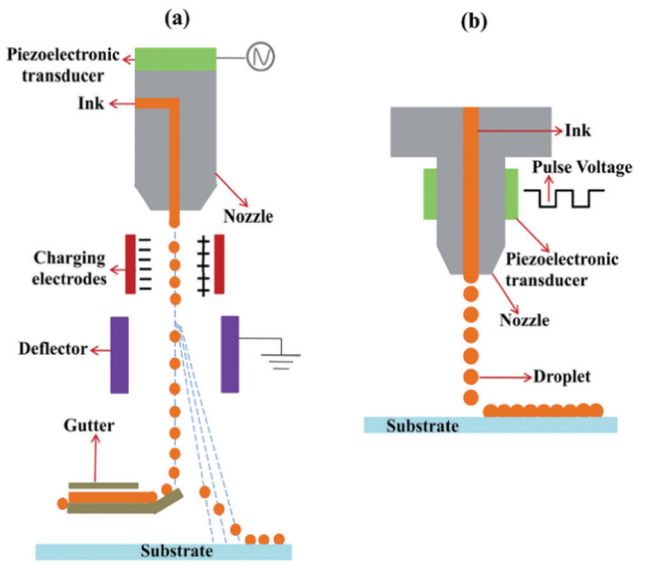

Fig. 2 Schematic illustration of two kinds of inkjet printing methods: (a) CIP and (b) DoD inkjet printing. Adapted with permission.[67] Copyright 2019, The Royal Society of Chemistry.

CIP is a non-stop flow ejection through the nozzle. The ink fluid is firstly ejected from the nozzle and breaks into a column of droplets owing to Rayleigh instability. Then, with droplets falling down, they are partly charged by a pair of parallel charging electrodes. The charged droplets are influenced by the dual effect of gravity and electric force, steering towards the targeted position to form patterns. DoD inkjet printing is a more popular method compared with CIP owing to less ink waste and more precise pattern resolution. It can achieve 5000 dots per inch with fine adjustment of the nozzle diameter in the range of 20–100 μm.[46] Droplet formation is controlled by a sudden chamber volume change, digitally controlled by mechanical deformation of a piezoelectric transducer or mechanical collapse of thermal bubbles. As a result, DoD inkjet printing can be divided into piezoelectric and thermal DoD inkjet printing.

Ink formulation is important for inkjet printing, which is highly related to the formation of stable droplets. A dimensionless parameter Z is adopted to characterize the formation of a stable droplet:

$$Z = \frac{1}{\mathrm{Oh}} = \frac{\mathrm{Re}}{\sqrt{\mathrm{We}}} = \frac{(\rho\alpha\gamma)^{0.5}}{\eta}, \quad (2)$$

where Oh is the Ohnesorge number, Re is the Reynolds number, We is the Weber number, η is the dynamic velocity, ρ is the density, γ is the surface tension, and α is the characteristic length.[67] Reis and Derby adopted numerical simulations to characterize the drop formation. The Z value of printable fluids is in the range of $1 < Z < 10$.[68] When $Z < 1$, the fluid is too viscous and it is difficult to form a stable droplet. When $Z > 10$, surface tension dominates and the fluid is not stable, accompanied by satellite droplet formation. Generally, the inks are required to have low viscosity (4–30 cP) and high surface tension (typically >35 mN m^{-1}) to generate a stable stream of droplets.[45] Besides, the interaction between the substrate and droplets is also important to determine the film formation, *e.g.* surface roughness, surface wetting, and the contact angle of a drop on the substrate.

2.1.2 Contact fabrication. Blade coating is regarded as an alternative to spin coating in small-area device fabrication and as the first-step attempt towards large-area device fabrication (Fig. 1e). Compared with spin coating, blade coating has a high material utilization ratio ($>95\%$) and fits R2R fabrication (*e.g.* knife coating, a version of blade coating). A blade with a certain distance (usually 10–500 μm) above the substrate linearly drags the ink on the substrate to form a homogeneous thin film. The film thickness is related to the distance between the substrate and blade, substrate surface energy, ink surface tension, ink viscosity, and the speed of the blade. The final film thickness is expressed by:

$$d = 0.5\left(g\frac{c}{\rho}\right), \quad (3)$$

where d is the film thickness, g is the gap distance between the blade and substrate, c is the concentration of the ink, and ρ is the density of the material in the final film. Generally, the blade

speed is in the range of 1–100 mm s^{-1}. When the ink is sticky, the blade speed is relatively slow. Meanwhile, the dissolved material might aggregate or crystallize during film formation, which restricts the further development of upscaling fabrication.

Screen printing is a versatile printing technology, suitable for 2D patterning of printed layers. It uses a steel mesh or an artificial fiber screen. There are many empty areas on the screen, which can be filled by the deposited ink. A squeegee linearly moves along the screen, pressing the ink onto the empty areas to form patterns. As a result, the layer thickness is correlated with the screen volume, which can be empirically expressed as

$$d = V_{\text{screen}} k_{\text{p}} \frac{c}{\rho}, \quad (4)$$

where d is the film thickness, V_{screen} is the screen volume, k_{p} is the material pick-out ratio, c is the solid material concentration of the solution, and ρ is the material density of the deposited film. A relatively high viscosity, varying from 50 to 5000 cP, is required for screen printing to avoid ink flow between empty areas on the screen. Ideal viscosity behavior is a high static viscosity and a low shear viscosity with a short viscosity recovery time. The ink should not be dried during ink flowing and film formation, and therefore a low volatility of the ink is required.[69] Generally, the film thickness is 10–500 μm, which is relatively thicker than the films achieved by other printing technologies. Thus, screen printing is suitable for fabrication of metallic electrode layers, such as silver and aluminum. According to the different requirements, screen printing can be divided into rotary screen printing and flat-bed screen printing (Fig. 1f and g). For the rotary screen printing, the screen is cylinder-shaped with a squeegee inside. The substrate rolls outside the printing roller, supported by a backup roller. Because the printed ink is surrounded by a closed printing roller, the volatility can be relatively higher. For flat-bed screen printing, it contains a fixed pattern mask, and the ink can be pushed through the empty areas on the mask to contact with the substrate by a squeegee. Due to strict requirements for the deposited ink and equipment, flat-bed screen printing is regarded as a tentative scalable technology, suitable for lab upscaling trials.

2.2 Series-substrate fabrication

2.2.1 Substrate transport type. According to different product requirements, series-substrate transport production lines can be classified into R2R, sheet-to-sheet, sheets-on-shuttle and roll-to-sheet (Fig. 3).[70] In large-area OSC production, R2R processing is more suitable for high-speed fabrication and delivers high pattern accuracy. R2R processing is also known as reel-to-reel or web-fed printing technology. Generally, a R2R system is composed of an infeed unit, a printing unit, a drying unit, a cutting unit, a folding unit, and more. The infeed unit peels the web off the roller and adjusts the web speed to the printing machine. Then the web passes through the printing roller and drying roller with hot air and ultraviolet and near-infrared light irradiation. At the end, the web passes through a cooling roller and is recollected by a new folding roller. Compared with the other three types of transport

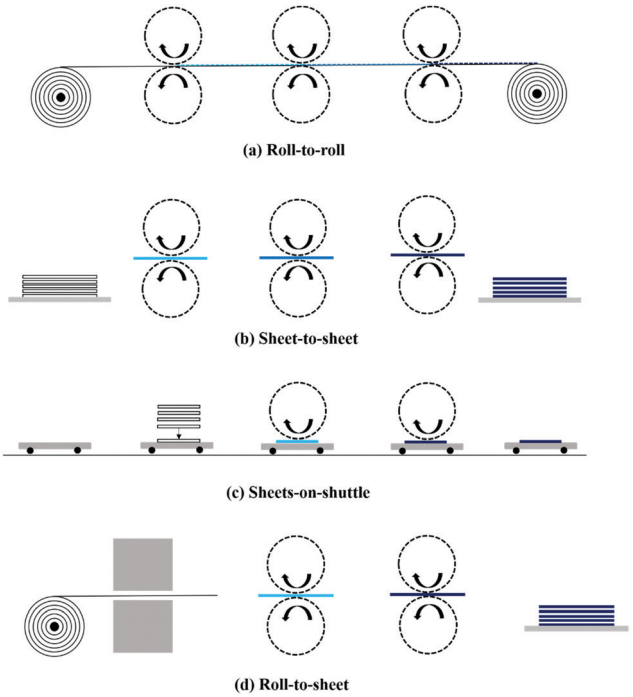

Fig. 3 Illustration of substrate transport types. Reproduced with permission.[70] Copyright 2014, the authors, under the CC BY-NC-ND 3.0 license.

production lines, the R2R system has two advantages. First, the R2R system is relatively simple which is convenient for lab-scale trials. Second, the R2R system is a continuous process which can effectively reduce the fabrication time in practical fab-scale fabrication. In addition to R2R, the other three production lines are rarely used in large-area OSCs. The sheet-to-sheet process, which is also known as the sheet-fed process, is more suitable for desktop-based trials. The sheets-on-shuttle substrate transport process transports substrates without double cylinder impression, which is suitable for sensitive materials (like DVD discs). The roll-to-sheet process combines the advantages of R2R and sheet-to-sheet. However, this method is high-cost and not mature up to now.

2.2.2 R2R fabrication technology. Generally, R2R-compatible fabrication technologies are contact type, including knife-over-edge coating, slot-die coating, gravure printing, and flexographic printing (Fig. 4). Some special R2R-compatible fabrication technologies, *e.g.* the floating film transfer method, are newly developed.

Knife-over-edge coating is a zero-dimensional coating method, similar to blade coating, in which the knife is fixed at a certain distance towards the supporting roller and the web is moving (Fig. 4a). Excessive ink is gradually added to a bath downstream of the knife.

Slot-die coating is a one-dimensional coating technology, in which one or more stripes with well-defined widths can be formed (Fig. 4b), and can meet the demand of a high degree of patterning in upscaling fabrication. The ink is supplied by a pump or a pressure system to a steel-made coating head, and it is deposited through a well-patterned mask to the moving substrate.

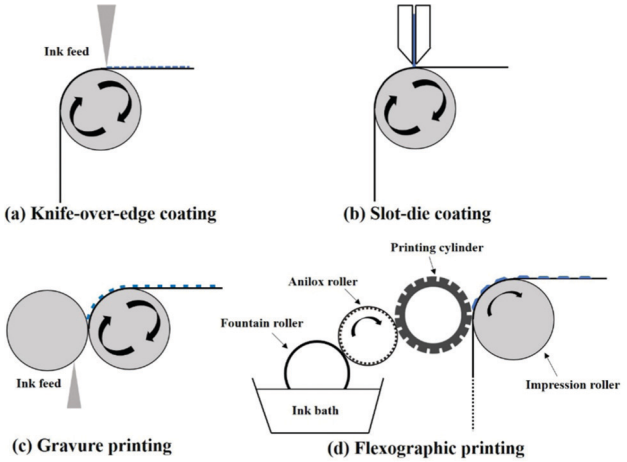

Fig. 4 Series-substrate fabrication technologies. Reproduced with permission.[47] Copyright 2020, the authors, under the Creative Commons Attribution 3.0 license (b). Reproduced with permission.[45] Copyright 2009, Elsevier (a, c and d).

The most important part in a slot-die head is a well-designed mask defining the slots and voids in the coating head. Generally, the slot-die head is equipped with a meniscus guide, which is used to control the striped pattern and edge quality of different layers. Fig. 5a shows a well-patterned coating mask with a meniscus guide comprising 5 stripes with a width of 12 mm spaced at 3 mm.[71] The mask thickness is usually in the range of 20–50 μm. Another important component is the pump system. Peristaltic and piston pumps are used for inks with low viscosity (such as organic active layer and ZnO nanoparticles), and pressure tank pumps are used for relatively viscous pastes (such as Ag pastes).[72]

In order to get a well-distributed large-area film, forming a standing meniscus which lies between the moving substrate and coating head is important (Fig. 5b).[73] Generally, slot-die coating is forgiving in ink viscosity. The ink solution usually possesses a low viscosity in the range of 1–20 cP. When using relatively viscous solutions (>100 cP), adopting a high coating speed (>10 m min^{-1}) is a useful method to get a standing meniscus. Besides, adjusting the liquid feeding rate, ink flow rate, and ink concentration can work as well. The film thickness can be expressed as follows:

$$d = \frac{f}{Sw} \times \frac{c}{\rho}, \quad (5)$$

where d is the film thickness, f is the ink flow rate, S is the substrate speed, w is the width of the pattern, c is the ink concentration, and ρ is the density of the dried ink material.

Gravure printing is a more complex version of knife-over-edge coating and offers high-throughput, high-resolution, and high-quality patterning (Fig. 4c). It contains two rollers, a coating roller with an engraved pattern and a support roller with guiding the web. Generally, the print patterns are engraved into the coating roller through laser patterning, chemical etching or electromechanical etching. A high resolution of 20 μm can be realized. In a continuous R2R system, the coating roller is partly inserted into an ink bath. As the coating roller rotates in the ink bath, the engraved cells can be filled with ink. Excessive ink is knifed off the roller. While the coating roller is contacting with the support roller, the ink is transferred from the gravures onto the substrate under high printing pressure (usually 1–5 MPa). The efficiency of gravure printing is highly related to printing parameters (printing speed, printing pressure), engraved coating roller parameters (cell volume, cell depth, wall width, channel width, tone, screen angle, line density and stylus angle) and ink properties.[74–77] Among the engraved coating roller parameters, line density is the most important parameter for thickness control. The lower the line density, the larger the cell volume and the thicker the film. Compared with other printing methods, gravure printing is suitable for low-viscosity ink solutions (10–1000 cP), high-speed processing and 2D patterning.

Flexographic printing is a 2D patterning technology which is an analogue of gravure printing. The ink transfer is performed from a relief opposed to cavities and the final pattern is formed over the printing plate. Typical flexographic printing is composed of four rollers (Fig. 4d). A fountain roller is partly immersed in the ink bath and touches an anilox roller, which has a well-defined engraved pattern. After that, the ink is transferred from the anilox roller to the printing roller, and then from the printing roller to the impression roller. This continuous R2R setup has similar advantages and limitations to gravure printing. Gravure printing and flexographic printing technologies have different application situations. The main differences between gravure printing and flexographic printing include the ink transfer pathway, printing speed, printed stripe thickness and ink viscosity. Flexographic printing uses a plate with a raised surface and fast drying fluid inks to print directly onto the desired substrate. Gravure printing

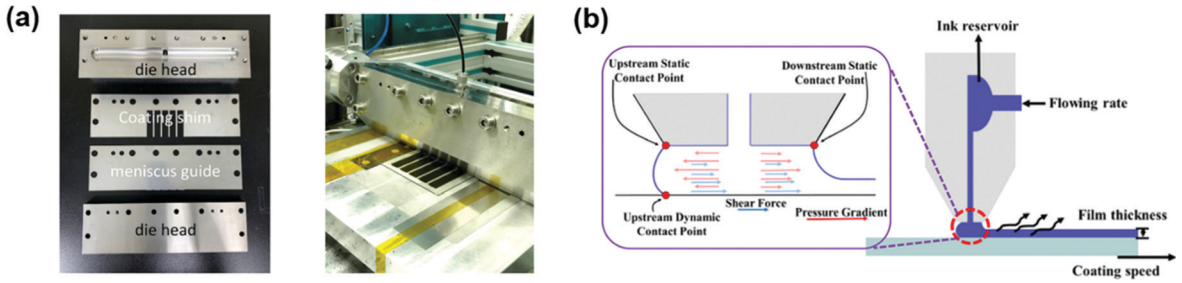

Fig. 5 (a) A slot-die coater equipped with a coating shim and a meniscus guide. Adapted with permission.[71] Copyright 2019, Elsevier. (b) Illustration of the stable meniscus formed. Adapted with permission.[73] Copyright 2019, Elsevier.

Table 1 Comparison of coating and printing technologies

Technique	Ink waste	Pattern[a]	Speed	Ink viscosity	Contact
Casting	Low	0	—	Low	No
Spin coating	High	0	—	Low	Yes/no
Spray coating	Medium	0	Medium	Medium	No
Inkjet printing	Low	2	Medium	Low	No
Blade coating	Low	0	Low	Low	Yes
Screen printing	Low	2	Medium	High	Yes
Knife-over-edge coating	Low	0	Medium	High	Yes
Slot-die coating	Low	1	High	Relatively high	Yes
Gravure printing	Low	2	High	Relatively low	Yes
Flexographic printing	Low	2	High	Relatively low	Yes
Floating film transfer	Low	0	High	Medium	Yes

[a] Pattern: 0 (0-dimensional); 1 (1-dimensional); 2 (2-dimensional).

is an intaglio printing process. The print patterns are engraved into the coating roller, and when the coating roller is contacting with a support roller, the ink is transferred from the gravures onto the substrate under high printing pressure. Furthermore, flexographic printing exhibits a slower printing speed (*ca.* 500 m min^{-1}) compared with gravure printing (*ca.* 1000 m min^{-1}), as well as thinner printed stripes (<1 μm in flexographic and ≈ 1 μm in gravure). The ink viscosity in flexographic printing (*ca.* 50–500 cP) is usually lower than that used in gravure printing (*ca.* 100–1000 cP).[78] Flexographic printing is suitable for inks with high volatility because there is a closed ink chamber.

The floating film transfer method is an ultrafast, scalable and versatile printing technology for forming high-quality organic films by utilizing the Marangoni effect.[79–82] A polymer solution with a low surface energy is self-spreading at the water interface with a high surface energy. The spontaneous spreading is called the Marangoni flow. The spreading coefficient (S) dictates the spreading flow:

$$S = \gamma_1 - \gamma_2 - \gamma_{12}, \quad (6)$$

where γ_1 and γ_2 are the surface tensions of the substrate and polymer solutions, respectively, and γ_{12} is the interfacial surface tension between the two solutions. If S is positive, the polymer solution will spread automatically. The spreading film can be transferred to various substrates, including polydimethylsiloxane, PET, paper and so on. Furthermore, this method can be employed in R2R production lines.[83]

Here, we summarize the different characteristics of coating/printing technologies discussed above (Table 1), in terms of ink waste, pattern, coating/printing speed, ink viscosity requirements and contact between ink and substrates.

3. Large-area fabrication: equipment and module design

3.1 Production equipment

Lab-to-fab upscaling requires not only scaling of fabrication technology, but also scaling of equipment. In the lab-stage, desktop-based systems are adopted to test new fabrication technologies. The model is of a small size and can be put into a glove box for nitrogen atmosphere protection conditions.

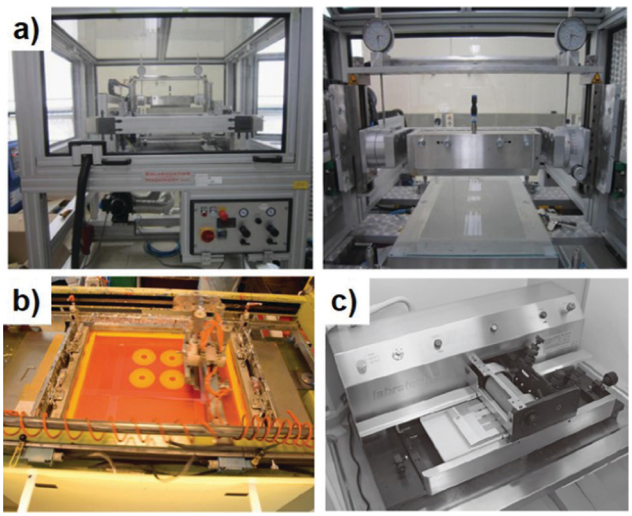

Fig. 6 (a) Easy Coater (Solarcoating Machinery Gmbh, left) and slot-die head (right). Adapted with permission.[84] Copyright 2013, Elsevier. (b) Flatbed screen printing machine. Adapted with permission.[85] Copyright 2009, Elsevier. (c) Schläfli Labratester table-top gravure printing machine. Adapted with permission.[86] Copyright 2010, Elsevier.

Fig. 6a–c show lab-scale flatbed coating systems for slot-die coating, screen printing, and gravure printing machines, respectively.[84–86] For example, Lee *et al.*[84] conducted a desktop-based lab-scale slot-die coating system with an equipment of Easy Coater (Solarcoating Machinery Gmbh, Germany). The coating speed varies from 0.3 to 5.0 m min^{-1}, and the temperature of the substrate can be controlled by applying extra heat to the vacuum plate. Krebs *et al.*[85] adopted a flatbed screen printing system to fabricate over 2000 modules in 63.3 hours (Fig. 7). Generally, the drying unit and the encapsulation unit are separated from the printing unit. These desktop-based small machines can realize a very high production speed with sheet-to-sheet printing. For example, Nelson *et al.*[87,88] adopted a Schläfli Labratester table-top gravure printing machine to realize fast sheet-to-sheet fabrication. The speed of gravure printing proofers is 40–60 m min^{-1}. The drying time varies from several minutes to hours. Because desktop-based testing machines lack the integration of the printing unit and drying unit, it cannot be directly used in a R2R-based system.

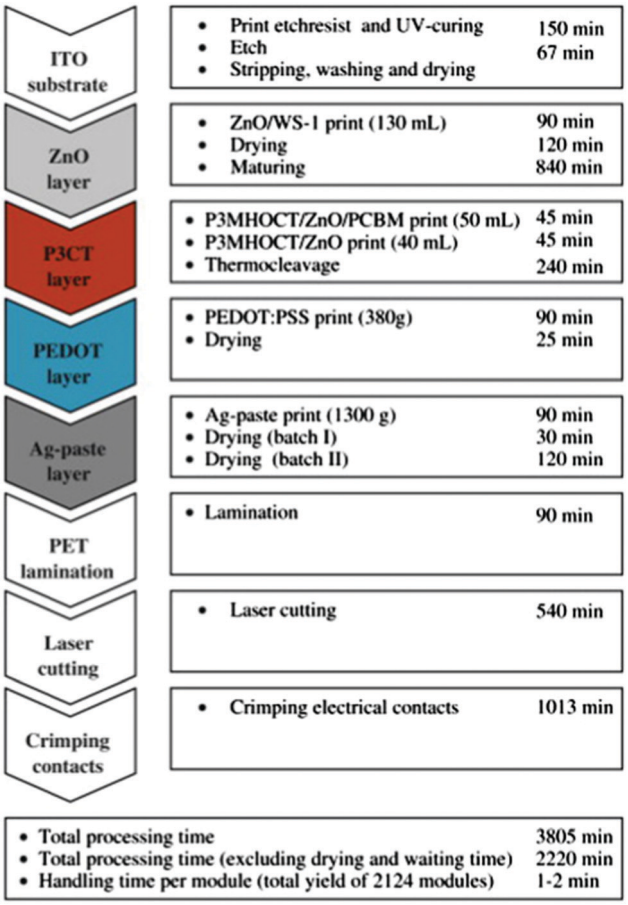

Fig. 7 A process flow chart outlining all the steps employed in a flatbed screen printing system. Adapted with permission.[85] Copyright 2009, Elsevier.

The development of R2R-based systems is divided into three stages: mini single roll-coater, mini R2R coater, and large-scale R2R machine. The mini single roll-coater was invented by Krebs' group (Fig. 8a), which mimics the coating performed on scalable R2R processing.[89] The system is composed of a drum rolling (diameter = 300 nm), a servomotor (speed varies between 0 and 2 m min^{-1}), a slot-die coating head (dead volume is less than 50 μL) and a syringe pump system. The rolling drum is automatically heated (up to 140 °C) to meet the demand of film drying and film post-annealing. Fig. 8b shows an improved version of the above-mentioned equipment. Krebs *et al.*[90] assembled a slot-die coater and a flexographic printer into one mini-roller setup and realized full solution processing. Interfacial layers and the active layer were printed using a slot-die coater, and the back electrode (Ag pastes) was fabricated by flexographic printing. This kind of mini roll coater is successfully employed to test new organic materials.[91,92]

The next stage is improving web width and printing speed, in which the printing unit and the drying unit should be integrated into one production line. The solar-1 coating line from Grafisk Maskinfabrik is the first fully automated R2R production line. It consists of a web alignment feedback control unit, a gravure and flexographic printing unit, a slot-die coating unit, and two integrated heating ovens (Fig. 8c).[93] In this equipment, film deposition and in-line thermal post-treatment can be realized in a single printing cycle. This machine allows fast printing with a speed of up to 30 m min^{-1} and a web width of 300 mm. Furthermore, Krebs *et al.*[94] upscaled the commercial mini roll coater and developed a lab-scale R2R processing machine, which is composed of a R2R inline machine, a testing machine, a UV-laminator machine, and a laser cutting machine (Fig. 8d). The whole system can handle the sample with a width of 305 mm at a coating velocity of 1–20 m min^{-1}. This system is compatible with *in situ* grazing incidence small angle X-ray scattering (GISAXS) testing and morphology analysis.

Considering modules or high-throughput products are usually serially connected, characterization and optimization

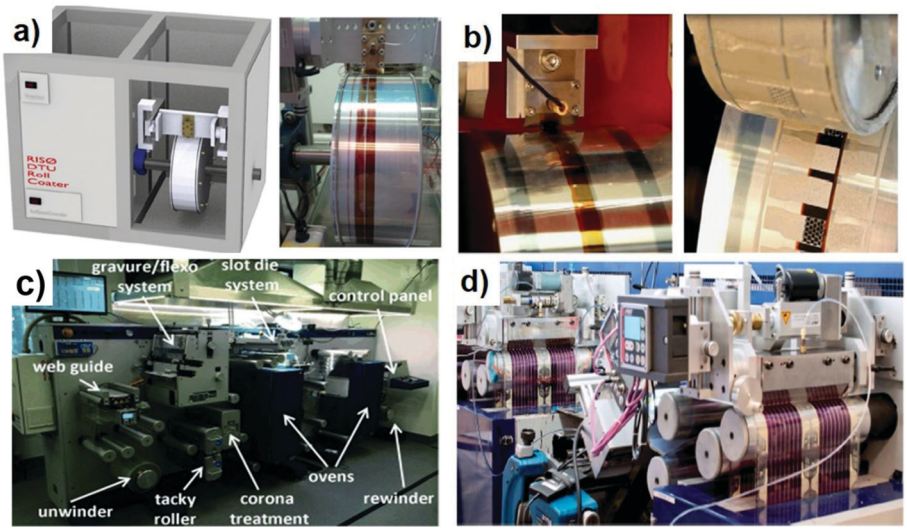

Fig. 8 (a) A mini-roll coater from Technical University of Denmark. Adapted with permission.[89] Copyright 2012, Elsevier. (b) A slot-die coater and a flexographic printer integrated into one mini-roller setup. Adapted with permission.[90] Copyright 2013, Elsevier. (c) Solar-1 coating line from Grafisk Maskinfabrik. Adapted with permission.[93] Copyright 2015, Wiley-VCH Verlag GmbH & Co. KGaA. (d) A fab-scale R2R printing and coating machinery. Adapted with permission.[94] Copyright 2014, The Royal of Society Chemistry.

of film morphology are difficult. Thus, it is a challenge to detect all the defects in a short time, especially under the condition of a high processing speed (>30 m min^{-1}) in large-scale R2R fabrication. *In situ* GISAXS measurement is an effective method for morphology analysis of each single device. For example, Andreasen *et al.*[95] developed an X-ray set-up where the coater unit is an integrated part of the small angle X-ray scattering instrument measurements. Using this system, the crystallization behavior of P3HT, both ordered edge-on orientation and unordered structure, can be easily observed (Fig. 9a). They further designed a micro R2R system, which adopts synchrotron X-ray light as the testing source, and a mini slot-die head and a syringe pump system as the printing unit components (Fig. 9b).[96] This system was used to document the formation of different functional layers in organic tandem solar cells. Some other methods, *e.g.* light-beam induced current (LBIC) mapping,[97] photoluminescence imaging, electroluminescence imaging,[98] and dark lock-in thermographic imaging,[99] are also adopted to evaluate the functionality of large-area OSC devices or modules. For example, Jørgensen *et al.*[100] employed LBIC technology to investigate three different kinds of silver inks as printed top electrodes. According to the current generated between the silver electrode and bottom ITO electrode, the difference of three silver inks was clearly shown in LBIC images. Quiles *et al.*[101] employed photoluminescence imaging and LBIC mapping to observe the donor and acceptor distribution in the active layer and reveal the relationship between PCE and cell length in laser-patterned modules. The 1.1 cm^2 module based on PBDTZT-*stat*-DBTT-8:4TICO showed a high geometrical fill factor (GFF) over 90%, a narrow interconnection length down to 300 μm and a high PCE of 4%.

The third stage is the large-scale R2R machine production line. It generally has typical web widths over 300 mm. The speed range is wide to allow a long drying time at a low drying speed. A series of processing units are assembled in an inline configuration, including an unwinding and in-feeding system unit, a printing and coating unit, a drying unit (hot air, near-infrared light, lasers, microwaves and intense pulsed light) and an out-feeding and rewinding unit. This large-scale R2R production line is customized by a few companies around the world such as Armor, Eight19, infinityPV, Oxford PV, FOM Technologies and Grafisk Maskinfabrik.

3.2 Module design

Up-scaling high-performance single devices towards high-performance modules is important for large-area device fabrication. As device area increases, the film homogeneity changes, which might induce local defects and decrease the photovoltaic performance of devices. A module is a series of single devices connected and is an effective method to avoid film morphology inhomogeneity during up-scaling. An OSC module is composed of series-connected single devices (Fig. 10) and typically involves

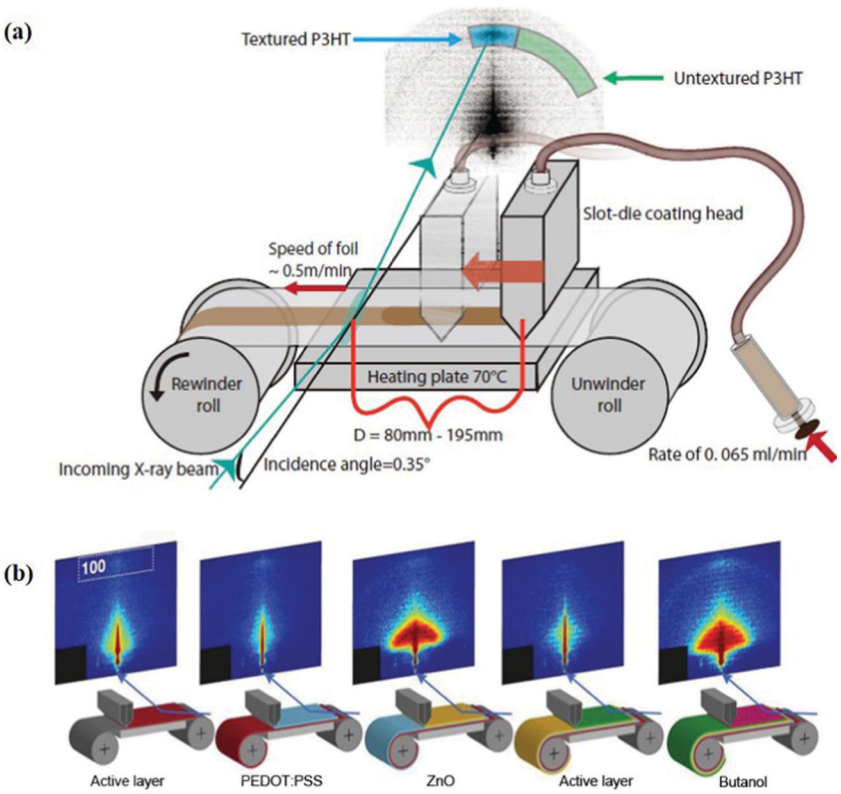

Fig. 9 (a) An X-ray set-up where the slot-die coater unit is an integrated part of the small angle X-ray scattering instrument measurements. Adapted with permission.[95] Copyright 2014, the authors, under the Creative Commons Attribution 3.0 Unported license. (b) An *in situ* R2R X-ray scattering measurement used for tandem OSCs. Adapted with permission.[96] Copyright 2015, Wiley-VCH Verlag GmbH & Co. KGaA.

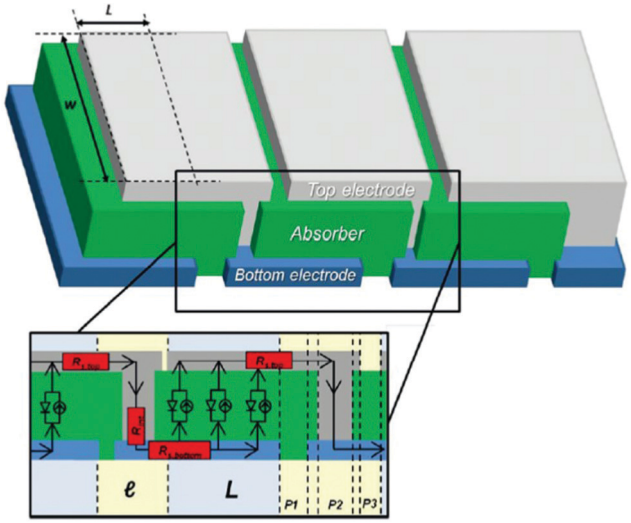

Fig. 10 Diagram of module fabrication. Adapted with permission.[50] Copyright 2015, Wiley-VCH Verlag GmbH & Co. KGaA.

three laser ablation processing steps P1, P2 and P3. P1 achieves structuring of the bottom electrode, such as ITO. The P2 scribe goes through the two interfacial layers and active layer until the bottom electrode. Ideal P2 processing achieves a selective ablation of the active layer and interfacial layer without destroying the ITO layer. P3 achieves an isolated top electrode. The main challenge of whole laser patterning is selective ablation of top layers without damaging bottom stacks and decreasing the pattern gap as well. The interconnect patterning parts are incapable of generating photocurrent, which is called the dead area. The GFF is used to describe the effective area of modules, which is defined as the ratio of the active area to the total area of the module:

$$\mathrm{GFF} = \frac{\text{Active area}}{\text{Total area}} = \frac{n \times w \times L}{n \times w \times (L + l)} = \frac{L}{L + l}, \qquad (7)$$

where n is the number of single cells, w is the single cell width, and L and l are the lengths of the active area and dead area, respectively. The GFF should be as large as possible to reduce the geometric loss in a monolithically interconnected module. Brabec *et al.*[50] analyzed the relationship between the L, l and the module's PCE. Generally, it is difficult to achieve >90% GFF in a module. To solve this problem, precise technical skills with controllable physical and chemical processing are required. One solution is adopting high-resolution laser printing. It employs strong irradiation from a focused laser beam to remove materials from the surface. Tipnis *et al.*[102] adopted laser ablation to pattern modules of series connected cells and achieved 233 cm^2 total area OSC modules. In order to improve the GFF value, picosecond and femtosecond pulsed laser sources have been further developed. To produce 64 cm^2 modules based on the HDR14:C60 active layer, a ps-laser ablation system with a pulse duration of 6 ps at a wavelength of 1030 nm, a maximum pulse energy of 125 μJ and a beam quality factor M^2 of 1.2 was adopted by Röttinger *et al.*[103] This system exhibited a high GFF of 94% and a PCE of 4.3%. In order to further improve scribe quality, fs-pulsed lasers have been developed. Brabec *et al.*[104] adopted an ultrafast fs-laser ablation system, with a pulse duration less than 350 fs at a repetition rate of up to 960 kHz. By optimization of the laser fluence and the patterning overlap, the best modules had a total interconnection regime of 178 μm, a GFF of 83% and a PCE of 1.38% with ITO/aluminum-doped ZnO/P3HT:PCBM/PEDOT:PSS/Ag. Egelhaaf *et al.*[105] employed an ultrafast fs-laser ablation system to produce modules with an extremely high GFF of 98.5% consisting of 14 cells with an active area of 35 cm^2 and an interconnection width < 90 μm. Recently, Distler *et al.*[106] adopted a ns-laser ablation system to make two new certified world record efficiencies, 12.6% on a module area of 26 cm^2 and 11.7% on a module area of 204 cm^2. They carefully tuned laser ablation parameters and the module patterning sequence as follows: (1) they adopted ns-lasers instead of fs-lasers, which significantly improves product reproducibility and reduces investment cost; (2) considering different laser power demands of the ZnO transport layer and active layer, they divided the traditional P2 step into a P2 sequence of two steps and adopted different laser energies in order not to destroy the PM6:Y6:$PC_{61}BM$ active layer.

Except for traditional three-step laser patterning, several strategies have been developed to design new modules and achieve effective interconnection. To fabricate "invisible" modules, Egelhaaf *et al.*[107] developed a new strategy to achieve effective but visually inconspicuous interconnects with the combination of inkjet printing (Fig. 11a). In this approach, only top and bottom electrodes were patterned by a laser, and the P2 step was replaced by an Ag bridge. Highly conductive Ag bridges were printed onto the bottom electrodes, forming a conductive pathway to the top electrode. A freedom-shape OSC with 84 cm^2 achieved a 1.60% PCE with a high GFF of 95%. Lee *et al.*[108] designed a unique monolithic interconnection that enables efficient module fabrication without patterning the charge transport layers, considering that effective charge recombination occurs at the contacts between charge transport layers (Fig. 11b). By printing the ZnO and MoO_3 transport layers with a doctor-blade machine for non-patterned single-layer forms, and printing the active layer and Ag electrode with a slot-die machine for stripe patterning, they fabricated a 4.5 cm^2 module with a GFF of 90%. Yoo *et al.*[109] proposed a novel series-connected OSC module fabrication method (Fig. 11c). They designed some linear microstructures by printing a high-viscosity resin. These linear structures exhibited high-angle contact, which can form a separator/interconnect for series-connection devices. This novel module structure exhibited an extremely high GFF of 95.6%.

Another solution of increasing GFF and achieving next-stage arbitrary shaped OSC modules is adopting some high-resolution, 2D printing methods, such as inkjet printing, screen printing and gravure printing. Arbitrary shaped OSCs have higher requirements in the dimensional accuracy compared with traditional rectangular cells. Inkjet printing, screen printing and gravure printing exhibit drop-on-demand properties and accurate 2D printing, which are beneficial for arbitrary deposition of materials. For example, Groen *et al.*[110] fabricated a fully inkjet-printed 1 cm^2 OSC (six layers in total). They also fabricated an OSC in the shape of a Christmas tree, which demonstrates the advantage of freedom

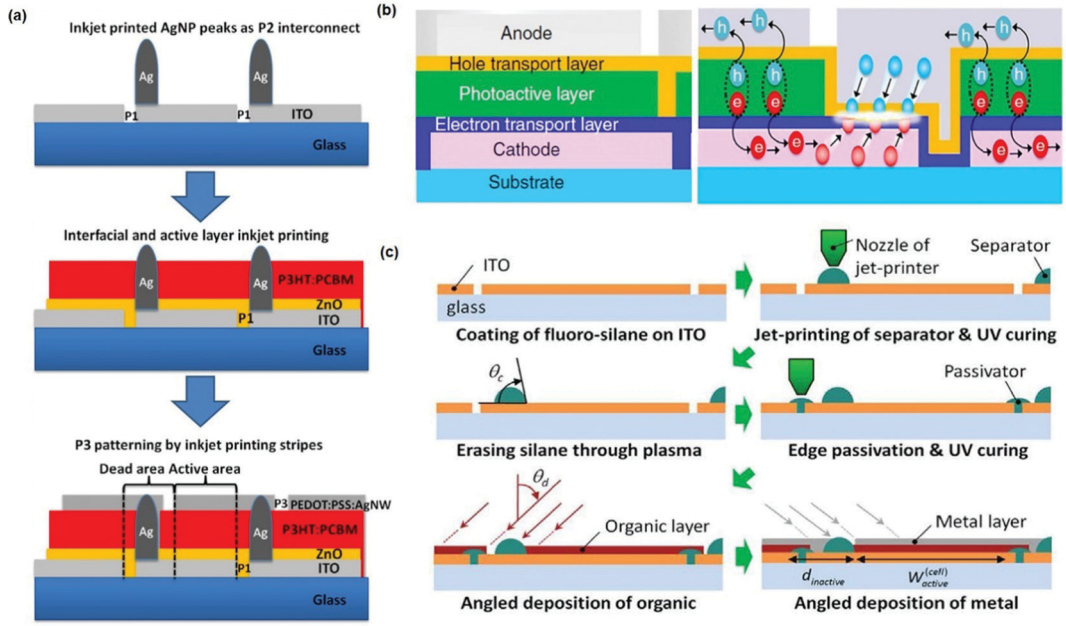

Fig. 11 (a) Schematic illustration of an OSC module fabricated by the inkjet printing method with hidden interconnects. Adapted with permission.[107] Copyright 2018, Wiley-VCH Verlag GmbH & Co. KGaA. (b) A special monolithic interconnection that enables efficient module fabrication without patterning the charge transport layers. Adapted with permission.[108] Copyright 2016, the authors, Creative Commons Attribution 4.0 International License. (c) Schematic illustration of a special OSC module design with addition of fluoro-silane. Adapted with permission.[109] Copyright 2014, Elsevier.

of design for the inkjet printing. Krebs *et al.*[42] fabricated a "Solar hat" module by screen printing. Sauermann *et al.*[111] adopted slot-die coating and screen printing to fabricate a "Solar Tree", displayed during the Milan EXPO 2015. Välimäki *et al.*[112] adopted gravure and rotary screen printing methods to fabricate a first "Solar Tree leaf", achieving the fabrication of arbitrary-shaped OSC modules.

4. Device component processing

The key components of OSCs are the active layer, the interfacial layer, and the electrodes, and all of them have specific requirements for fabricating high-performance large-area devices. Inks of each layer need to be adjusted to meet different requirements during processing. In this part, we will discuss the requirements and process optimization strategy of the printable active layer, interfacial layers and electrodes.

4.1 Active layer

For small-area devices, the wet active layer film is dried due to the centrifugal effect during spin coating. However, the film forming and drying behavior in other coating or printing methods is different. Considering that the traditional film morphology optimization strategy may not be adaptable for large-area device fabrication, it is of great importance to seek film optimization strategies for large-area device fabrication. At the same time, in the past decade, many efforts were focused on fabricating large-scale devices or modules based on fullerene acceptors. There are very limited studies focusing on non-fullerene acceptor based OSCs in upscaling printed devices or modules. Considering that non-fullerene acceptors exhibit different packing and aggregation behaviors compared to fullerene acceptors in large-area device printing processes, it is a challenge to find new strategies to optimize non-fullerene-based large-area OSCs. All the mentioned donor polymers and non-fullerene acceptors are shown in Fig. 12 and 13. Table 2 summarizes the printed non-fullerene OSCs discussed in this review. The efficiencies of large-area OSCs are summarized in Fig. 14.

Solvent engineering is an important strategy to adjust ink rheological properties and optimize the film morphology of large-area devices or modules. The fluidic properties of inks have a great influence on uniform film formation. For example, in inkjet printing, a printable fluid should have a dimensionless Fromm number Z value between 4 and 14 by considering characteristics such as single droplet formability, positional accuracy, and maximum allowable jetting frequency. Z is defined as follows:

$$Z = \frac{(\alpha\rho\gamma)^{1/2}}{\eta}, \quad (8)$$

where α is the radius of the printing orifice, ρ is the density, γ is the surface tension and η is the viscosity of the fluid.[113,114] In order to control the ink rheological properties, prepare a uniform film, and optimize film morphology, several methods based on solvent engineering strategies have been developed, *e.g.* the use of cosolvents, additives and more.

An effective method to adjust the ink rheological properties based on solvent engineering strategies is the use of cosolvents. A cosolvent can effectively control the ink behavior and eliminate the "coffee ring" formation. Generally, the cosolvent is composed

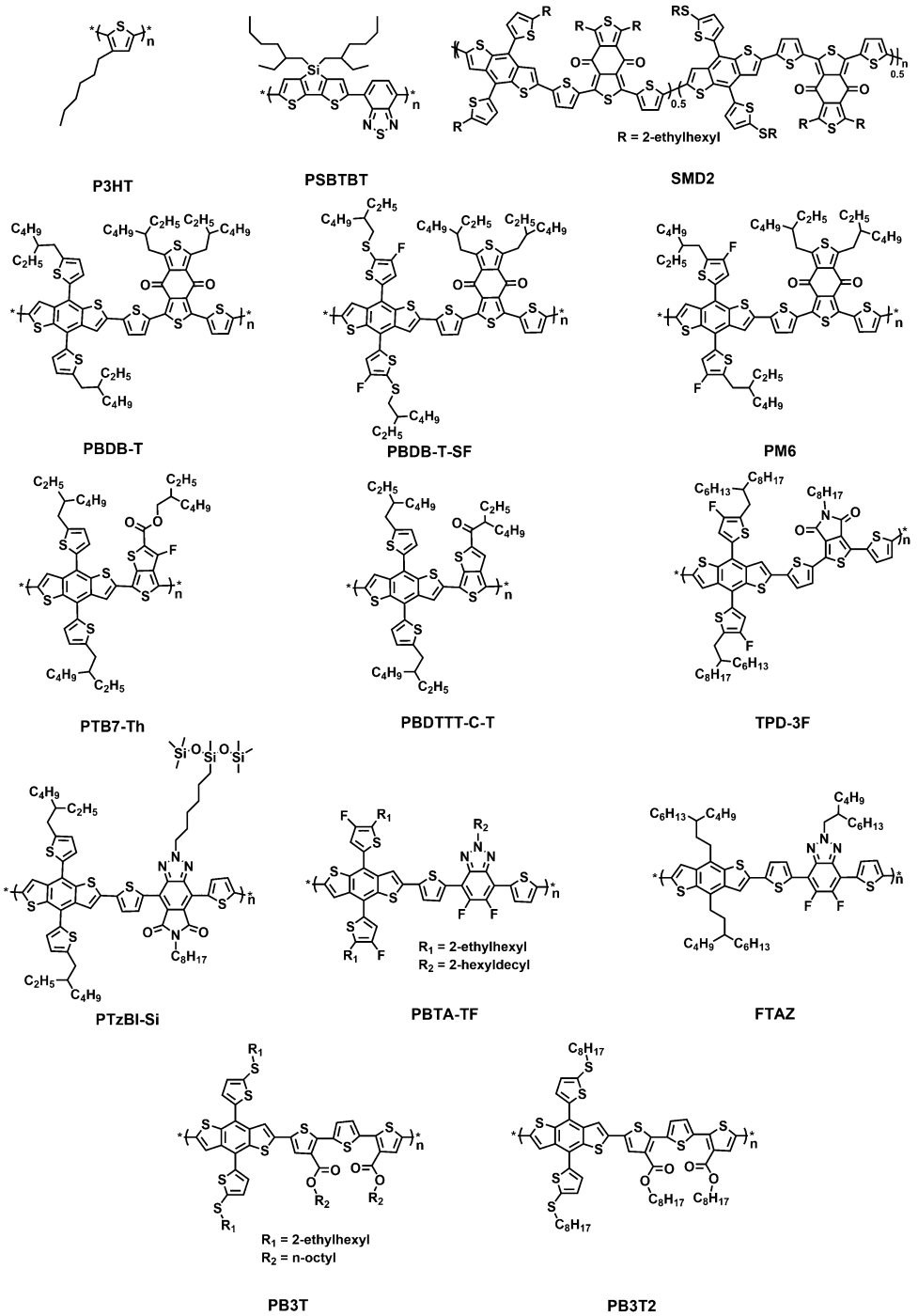

Fig. 12 Chemical structures of polymer donors involved in this article.

of two solvents with different boiling points. By adding a high boiling point solvent, there is a concentration gradient formed at the droplet surface. The counterclockwise Marangoni flow with an opposite movement direction towards the flow direction can prevent the particle segregation. Deng *et al.*[115] fabricated a PTB7-Th:FOIC-based electrospray-deposited OSC, which exhibited a PCE of 9.45%. The low-vapor-pressure non-halogen solvent *o*-xylene and the high-vapor-pressure solvent chloroform were employed to form a binary solvent system with an ideal evaporation speed, electrical conductivity and sufficient solubility. A longer droplet evaporation time with sufficient solubility can decrease the roughness and domain size of polymer/non-fullerene blend films. Hou *et al.*[116] fabricated PBTA-TF:IT-M-based devices processed with environmentally friendly cosolvents (tetrahydrofuran/isopropyl alcohol). A PCE of 11.7% was achieved by adopting the blade-coating method; for a larger area device with an area of 1.0 cm^2, a PCE of 10.6% was still maintained.

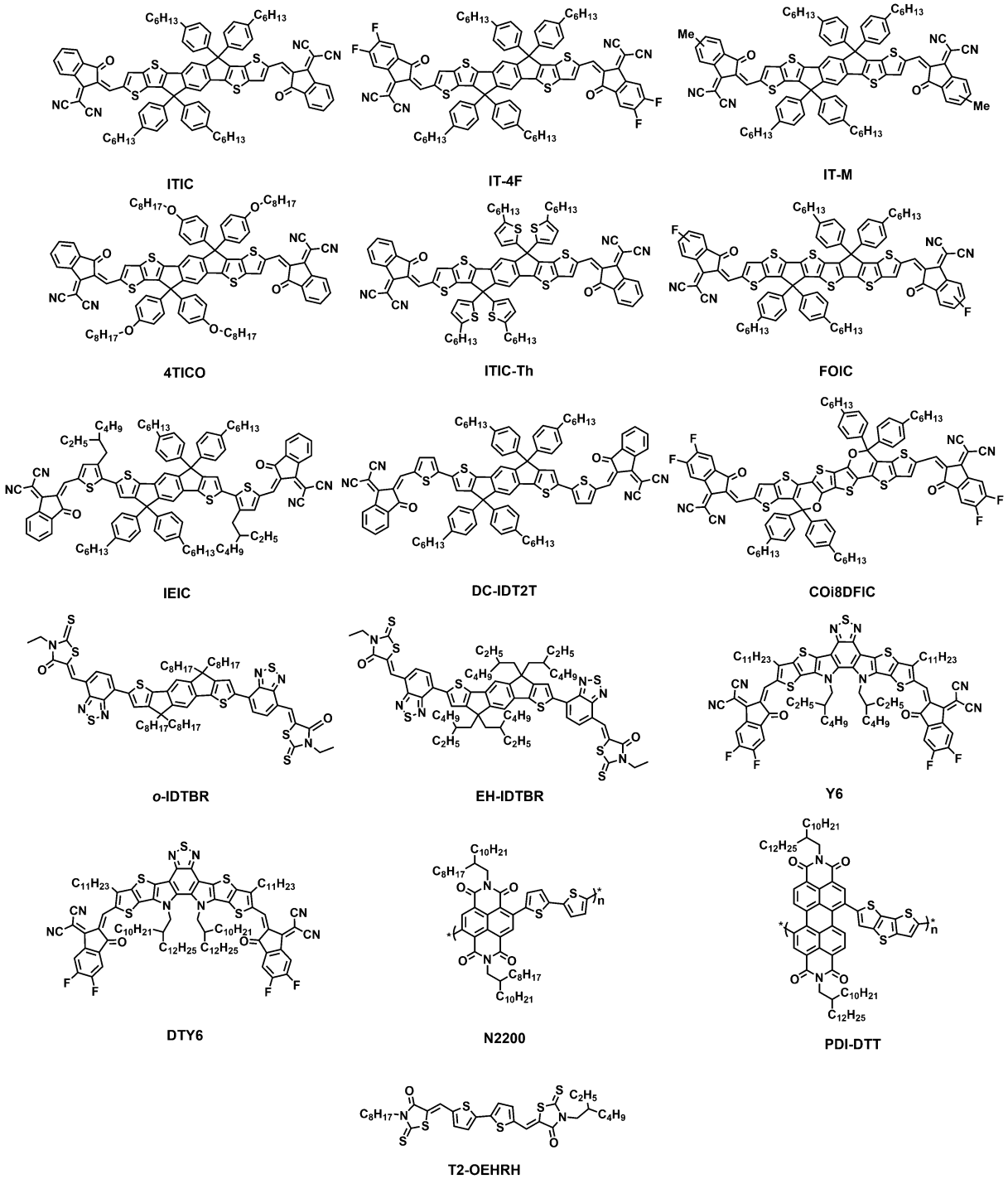

Fig. 13 Chemical structures of non-fullerene acceptors involved in this article.

An effective method to optimize the morphology of large-area OSCs is using proper additive reagents. Additives usually have different solubilities for the donor and acceptor, so donor/acceptor crystallinity and packing behavior can be optimized during film formation. For large-area printing processes, selecting proper additives is important. For example, Yuan *et al.*[117] investigated the influence of three additives, 1,8-diiodooctane (DIO), 1,8-octanedithiol (ODT) and 1-chloronaphthalene (CN), on the morphology of blade-coated PBDB-T:ITIC devices. Generally, DIO and CN are more beneficial and widely used in spin-coated devices. However, in the blade-coated device (4 mm^2), the ODT-based device not only exhibited the best performance with a PCE of 10.2% but also the best device stability. The ODT-based device yielded a slower degradation with retaining 77% of the initial PCE after 150 min light illumination than the DIO-based device (55%). In addition, the ODT-based large-area device

Table 2 Overview of printed non-fullerene OSCs

Active layer (deposition method)	Bottom electrode (deposition method)	Top electrode (deposition method)	Area (cm^2)	V_{OC} (V)	J_{SC} (mA cm^{-2})	FF (%)	PCE (%) (average)	Ref.
PBDB-T-SF:IT-4F (slot-die coating)	Glass/ITO (magnetron sputtering)	Al (thermal evap.)	0.10	0.88	20.6	71.7	13.0 (12.1)	73
PM6:Y6:$PC_{61}BM$ (blade coating)	Glass/ITO (magnetron sputtering)	Ag (thermal evap.)	26.2	9.82	1.75	73.5	12.6 (12.6)	106
			204.0	26.7	0.65	69.0	12.0 (11.7)	
PTB7-Th:FOIC (spray coating)	Glass/ITO (magnetron sputtering)	Al (thermal evap.)	0.05	0.70	21.7	62.0	9.45 (9.25)	115
PBTA-TF:IT-M (blade coating)	Glass/ITO (magnetron sputtering)	Al (thermal evap.)	1.00	0.95	17.1	65.0	10.6 (—)	116
PBDB-T:ITIC (blade coating)	Glass/ITO (magnetron sputtering)	Al (thermal evap.)	0.90	0.87	16.8	59.0	8.59 (—)	117
PBDB-T-SF:IT-4F (slot-die coating)	Glass/ITO (magnetron sputtering)	Al (thermal evap.)	6.25	0.87	19.5	52.0	8.95 (7.9)	118
PBDB-T:ITIC (blade coating)	Glass/ITO (magnetron sputtering)	Al (thermal evap.)	1.00	0.89	17.1	66.1	— (10.0)	119
FTAZ:IT-M (blade coating)	Glass/ITO (magnetron sputtering)	Al (thermal evap.)	0.07	0.95	16.8	66.1	11.0 (10.5)	120
			0.56	0.93	16.4	64.6	9.85 (—)	
PBDB-T:ITIC (slot-die coating)	Glass/ITO (magnetron sputtering)	Ag (thermal evap.)	0.10	0.88	17.5	64.9	10.0 (9.76)	121
	PET/ITO (magnetron sputtering)		0.10	0.88	17.0	58.6	8.77 (—)	
PM6:Y6 (slot-die coating)	Glass/ITO (magnetron sputtering)	Al (thermal evap.)	0.56	0.80	26.4	64.2	13.8 (13.6)	122
PM6:IT-4F (blade coating)	Glass/ITO (magnetron sputtering)	Al (thermal evap.)	0.56	0.83	19.3	67.6	11.4 (10.8)	123
P3HT:*o*-IDTBR (inkjet printing)	Glass/ITO (magnetron sputtering)	Ag (thermal evap.)	0.10	0.71	13.8	67.2	6.47 (6.11)	124
			2.20	0.72	14.1	47.0	4.76 (—)	
PBDB-T:ITIC (slot-die coating)	PET/ITO (magnetron sputtering)	Ag (thermal evap.)	1.04	0.86	17.0	65.2	9.77 (9.52)	125
			15.0	5.10	2.79	60.6	8.90 (8.64)	
PM6:IT-4F (blade coating)	Glass/ITO (magnetron sputtering)	Al (thermal evap.)	0.12	0.86	20.8	72.0	12.88 (12.34)	126
PM6:Y6 (spin coating)	Glass/ITO (magnetron sputtering)	Al (thermal evap.)	1.00	0.81	24.9	63.0	— (12.7)	129
PM6:IT-4F (blade coating)	Glass/ITO (magnetron sputtering)	Al (thermal evap.)	1.00	0.86	21.1	72.0	13.2 (12.3)	130
PB3T:IT-M (spin coating)	Glass/ITO (magnetron sputtering)	Al (thermal evap.)	1.00	0.98	15.6	66.0	10.1 (—)	131
PB3T2:IT-M (spin coating)	Glass/ITO (magnetron sputtering)	Al (thermal evap.)	0.04	0.94	17.8	63.0	10.6 (10.3)	132
PBDB-T:IT-M (blade coating)	Glass/ITO (magnetron sputtering)	Al (thermal evap.)	1.00	0.91	15.5	68.0	9.67 (—)	133
PM6:Y6 (spin coating)	Graphene&AgNWs/PH1000 (—)	Al (thermal evap.)	0.04	0.83	23.2	70.0	13.4 (13.2)	138
PBDB-T:IT-M (spin coating)	PET/PEDOT:PSS (drop casting)	Al (thermal evap.)	0.04	0.925	15.6	70.7	10.2 (10.1)	143
PTB7-Th:ITIC (blade coating)	Glass/ITO (magnetron sputtering)	Ag (thermal evap.)	0.14	0.83	16.0	71.0	9.54 (9.33)	144
	PET/Ag/TiO_x (thermal evap.)	PEDOT:PSS (spin coating)	2.03	0.81	14.7	63.0	7.60 (7.32)	
PM6:Y6 (spin coating)	PET/Em-Ag/AgNWs/AZO (spin coating)	Al (thermal evap.)	1.00	0.80	25.0	61.0	12.3 (—)	149
TPD-3F:IT-4F (blade coating)	Glass/ITO (magnetron sputtering)	Ag (thermal evap.)	20.4	4.45	3.9	60.5	10.4 (—)	151
PTB7-Th:COi_8DFIC:$PC_{71}BM$	PET/Ag grid/PH1000	Ag (thermal evap.)	1.0	0.69	26.7	65.8	12.2 (12.0)	152
(slot-die coating)	(slot-die coating)		25.0	3.46	4.93	59.1	10.1 (9.81)	
			50.0	6.85	2.54	51.9	9.05 (8.80)	
PM6:Y6:$PC_{71}BM$ (spin coating)	PET/Ag grid/AgNWs:PEI-Zn (blade coating)	Ag (thermal evap.)	10.1	0.81	23.56	66.0	12.6 (11.6)	153
			54.0	7.34	2.57	70.0	13.2 (—)	
PBDB-T:ITIC:$PC_{71}BM$ (blade coating)	Glass/ITO (magnetron sputtering)	Al (thermal evap.)	216.0	14.2	0.91	59.0	7.69 (7.15)	154
PTzBI-Si:N2200 (slot-die coating)	Glass/ITO (magnetron sputtering)	Ag (thermal evap.)	1.00	0.87	16.1	72.7	10.15 (9.48)	162
PM6:IT-4F (blade coating)	Glass/ITO (magnetron sputtering)	Ag (thermal evap.)	1.00	0.84	20.0	68.0	11.4 (11.0)	163
PM6:DTY6 (blade coating)	Glass/ITO (magnetron sputtering)	Ag (thermal evap.)	18.0	5.11	3.89	72.5	14.4 (13.7)	164
PTB7-Th:EH-IDTBR:T2-OEHRH (blade coating)	Glass/ITO (magnetron sputtering)	Ag (thermal evap.)	55.5	11.47	1.29	63.0	9.32 (—)	165
SMD2:ITIC-Th (slot-die coating)	PET/ITO (magnetron sputtering)	Ag (screen printing)	80.0	8.80	1.12	53.1	5.25 (—)	44
PBTZT-*stat*-BDTT-8 : 4TICO (blade coating)	Glass/ITO (magnetron sputtering)	PH1000 (blade coating)	1.10	2.89	2.95	45.7	3.9 (3.8)	101
PSBTBT:PDI-DTT (slot-die coating)	PET/ITO (magnetron sputtering)	Ag (flexo-bed screen printing)	4.20	0.37	1.92	28.9	0.20 (—)	155
P3HT:*o*-IDTBR (blade coating)	Glass/ITO (magnetron sputtering)	AgNWs (blade coating)	0.10	0.70	11.3	66.6	— (5.25)	156
			59.5	0.69	10.9	61.9	4.7 (4.5)	
PBDTTT-C-T:PDI-DTT (slot-die coating)	PET/Ag grid/PEDOT:PSS (flexographic, R2R)	Ag grid (flexographic, R2R)	1.00	0.63	2.5	42.5	0.73 (0.67)	157
PBDTTT-C-T:DC-IDT2T (slot-die coating)	PET/Ag grid/PEDOT:PSS (flexographic, R2R)	Ag (flexographic, R2R)	1.00	0.80	3.1	40.1	1.02 (1.00)	158
PTB7-Th:IEIC (slot-die coating)	PET/ITO (magnetron sputtering)	Ag (flexographic, R2R)	0.70	0.90	5.4	36.7	2.26 (2.05)	159
	PET/Ag grid/PEDOT:PSS (flexographic, R2R)		1.00	0.94	6.9	35.2	1.79 (1.60)	
PBDB-T:ITIC (slot-die coating)	PET/Ag (magnetron sputtering)	CPP PEDOT (slot-die coating)	7.14	0.86	12.0	49.0	5.5 (5.1)	169

($90\ mm^2$) exhibited a high PCE of 8.59%. Apart from additive types, the additive amount needs to be adjusted in large-area printed technologies, which is different from the amounts in lab-scale small-area spin coating technology. For example, slot-die printed OSCs with a device area of 6.25 cm^2 based on PBDB-T-SF:IT-4F as the active layer were fabricated with different amounts of DIO. The addition of 0.25 vol% DIO enhanced the average PCE from 3.5% to 7.9%, whereas at lower or higher DIO contents this positive effect is less pronounced.[118] The optimized additive amounts in active layers by spin coating (0.5 vol% DIO) and slot-die coating (0.25 vol% DIO) are different owing to differences in the rheological properties of inks, residual solvent

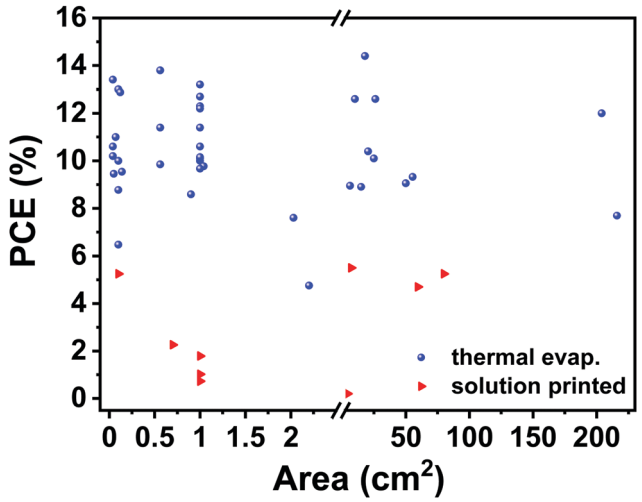

Fig. 14 Trend of PCEs with different areas of OSCs. The blue points represent the devices with thermally evaporated top electrodes and the red points represent the devices with solution printed top electrodes.

amount and solvent volatilization kinetics. Ma *et al.*[119] fabricated devices based on PBDB-T:ITIC by spin coating and blade coating with various DIO contents in air. A high average PCE of 10.03% was achieved for blade-coated devices with 0.25% DIO, higher than that of spin-coated devices with 1% DIO. The deviation in optimum DIO content in printed devices compared with spin-coated devices originates from the different active layer morphologies. The blade coating was found to induce crystal propagation along the direction of shearing. As a result, the partial role of DIO can be replaced by the blade coating technology, which decreases the DIO content in printed devices. In some cases, the additive amount in printed devices can be decreased even to 0%, which is beneficial for improving the device storage lifetime. Ade *et al.*[120] reported a non-fullerene OSC based on blade-coated FTAZ:IT-M as the active layer, and the active layer was processed under air conditions without solvent additives. This FTAZ:IT-M-based device yielded a PCE of nearly 11%. What is more, the storage stability of the device was improved, and this blade-coated FTAZ:IT-M device exhibited negligible performance loss after 20 days of aging in air.

Adjusting the temperature of the ink and substrate is another strategy to obtain uniform films and optimized morphology. Vak *et al.*[121] used a hot slot-die coating method (hot substrate of 120 °C and hot solution of 90 °C) to achieve high-performance ITIC-based 0.1 cm^2 devices. For slot-die coating, it is easy to accurately adjust the temperature of the slot-head (ink temperature) and the substrate towards a controlled thermodynamic state of the solution during the film formation. Through heating the slot-die head and substrate, the π–π stacking (010) distance decreased from 3.82 Å (ink temperature: 25 °C/substrate temperature: 25 °C) to 3.68 Å (90 °C/120 °C), leading to enhanced intermolecular interactions and charge transport. Using PEIE as an additional electron injection layer, a PCE of 10.0% was achieved, and PCEs of 8.8% and 7.1% were obtained *via* flexible substrate batching and roll-to-roll processing, respectively.

An active layer consisting of PM6 and Y6 received considerable attention recently. However, the temperature-dependent polymer PM6 has strong aggregation in widely-used high boiling solvents, *e.g.* chlorobenzene and 1,2-dichlorobenzene, and some hydrocarbon solvents, *e.g.* *o*-xylene and 1,2,4-trimethylbenzene, which limits upscaling. The hot temperature slot-die coating process can fix this problem. With the combination of a hot solution and a hot substrate, the slot-die coated PM6:Y6-based OSCs exhibited high PCEs of 15.2%, 15.4% and 15.6% processed by chlorobenzene, *o*-xylene and 1,2,4-trimethylbenzene, respectively. Large-area (56 mm^2) devices also exhibited high PCEs of 13.9%, 13.7% and 13.9% processed by chlorobenzene, *o*-xylene and 1,2,4-trimethylbenzene, respectively.[122]

Adjusting substrate temperature is also important for blade coating. For example, Ma *et al.*[123] varied the substrate temperature in blade-coated PM6:IT-4F devices to control the molecular ordering and phase separation (Fig. 15). The blade-coated devices with a low substrate temperature (30 °C) suffered from the low crystallinity of IT-4F and poor device performance. Through increasing the substrate temperature to 50 °C, a high PCE of 13.64% was achieved in air without any other processing treatments. Through grazing incidence wide angle X-ray scattering (GIWAXS) analysis, no scattering peaks of IT-4F at the low q location was observed in spin coating and blade-coating (30 °C) films, indicating the low crystallinity of IT-4F in these two blend films. A pronounced scattering peak was observed in the in-plane direction at q = 0.31 $Å^{-1}$ for blade-coating (50 °C) films, which is attributed to IT-4F backbone packing. For spin coating and blade-coating (30 °C) films, IT-4F molecules moved slowly, which results in weak crystallinity. With increasing temperature, molecular movement and arrangement of IT-4F had been triggered, resulting in the thermodynamic intermediate state of backbone packing. The charge transport along the backbone packing is fast, which is beneficial for PCE enhancement.

Adjusting substrate temperature also plays an important role in inkjet printing. For example, Baran *et al.*[124] reported a 0.1 cm^2 non-fullerene-based OSC *via* inkjet printing (Fig. 16). The device efficiency of the P3HT:*o*-IDTBR device by inkjet printing was 6.47%, comparable to that of spin coating. Furthermore, a 2.2 cm^2 turtle-shaped inkjet-printed device achieved a PCE of 4.76%. Through optimizing deposition temperature and drop spacing, common inkjet printing complications like nozzle clogging can be avoided. Fig. 16e presents the influence of deposition temperature and drop spacing on the homogeneity of active layer films. With increasing deposition temperature (>50 °C) and drop spacing (>15 μm), peaks and valleys can be clearly observed, which seriously decreased the device performance.

Adjusting the printing speed is another strategy to obtain a homogeneous film and optimized morphology. Chen *et al.*[125] investigated the relationship between the inking ratio and film morphological evolution in the slot-die coating active layer. The ratio of inking speed (0.10–0.20 mL min^{-1}) to stripping speed (0.10–0.15 m min^{-1}) is defined as the inking ratio, which describes the actual volume of ink printed per unit area. Excessive aggregation occurred in both low or high inking ratio-based films. Based on the device structure of PET/ITO/PBDB-T:ITIC/MoO_3/Ag, the PCE of this 1.04 cm^2 flexible device was 9.77%, and the PCE of the 15 cm^2

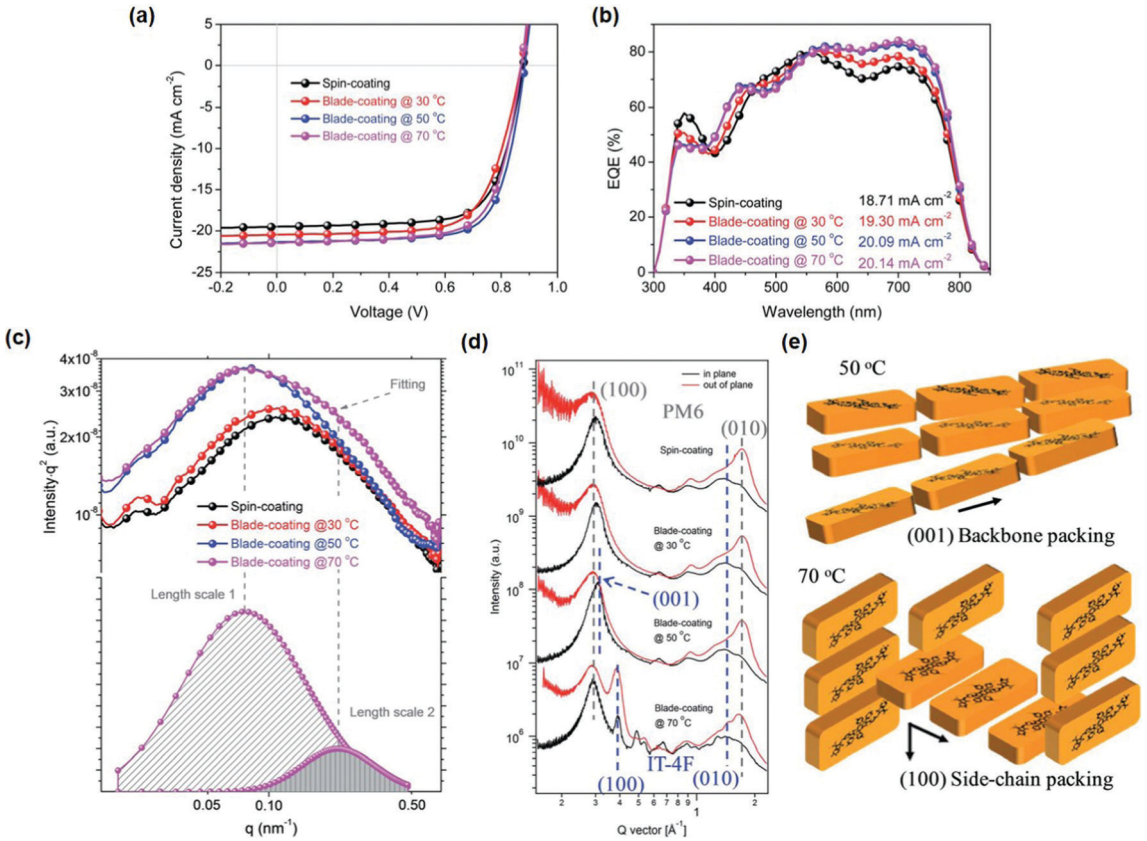

Fig. 15 (a) *J*–*V* curves, (b) EQE curves, (c) RSoXS profiles, and (d) GIWAXS line profiles of PM6:IT-4F devices based on spin coating and blade coating at 30, 50 and 70 °C. (e) The schematics of molecular packing for IT-4F molecules in the blend films prepared by blade-coating at 50 and 70 °C. Adapted with permission.[123] Copyright 2019, The Royal Society of Chemistry.

flexible device can still maintain 91% compared with the 1.04 cm^2 flexible device.

4.2 Interfacial layer

In order to promote large-area fab-scale OSC fabrication, all functional layers should be processed in scalable production technologies. High-quality printable interfacial layers with excellent thickness tolerance are important for large-area OSC fabrication. Generally, the active layer thickness is 100–300 nm, the interfacial layer thickness is 20–50 nm and the electrode thickness is 100–1000 nm. Considering the low thickness of the interfacial layer, a slight thickness variation may lead to significant performance deterioration. Thus, an ideal interfacial layer should meet the following requirements: high thickness tolerance, ultrahigh transparency in visible and near-infrared light regions, high electrical conductivity, superior charge carrier collection and transport properties, excellent chemical, thermal and photo-stability, suitable energy levels and low interfacial trap density.

As the cathode interfacial layer, ZnO is widely used owing to its high electron mobility, high visible light transparency and high thermal stability. The thickness and morphology of ZnO layers show great influence on the performance of printed devices. Ma *et al.*[126] investigated the influence of the surface morphology of ZnO interfacial layers on the performance of inverted OSCs with spin-coated and blade-coated active layers. The ZnO surface roughness exhibited a negligible influence on the optimized performance, performance uniformity and long-term stability of the spin-coated OSCs. However, the ZnO surface roughness significantly affected the performance and stability of the blade-coated devices. Compared with centrifugal forces in the spin coating method, the shear force in the blade-coating method is milder and the molecules had the tendency to precipitate during the slow drying process. The ZnO rough surface accelerated the precipitation process, leading to a poor contact between the interfacial layer and active layer. By using methanol-based ink to replace the acetone-based one, a smoother ZnO layer can be achieved; higher PCEs of 12.88% and 9.22% were achieved for the 0.12 and 1.04 cm^2 doctor-bladed PM6:IT-4F OSCs. By sensitizing ZnO nanocrystals with a conjugated polymer (poly(9,9-bis-(6′-diethoxyphosphorylhexyl)fluorene) (PFEP)), Zhang *et al.*[127] fabricated a printable highly conductive cathode interfacial layer. PFEP has dual effects. On one hand, PFEP polymer chains can assemble on ZnO surfaces *via* their pending phosphonate groups, leading to the formation of a uniform and smooth film during solution processing; on the other hand, charge transfer can occur between ZnO and PFEP, which improves the conductivity of the interfacial layer. By blade coating, a PCE of 6.26% was achieved in P(IID-DTC):$PC_{71}BM$-based OSCs with a device area of 12.5 mm^2. To fabricate large-area (1 cm^2) inverted OSCs *via* R2R micro-gravure

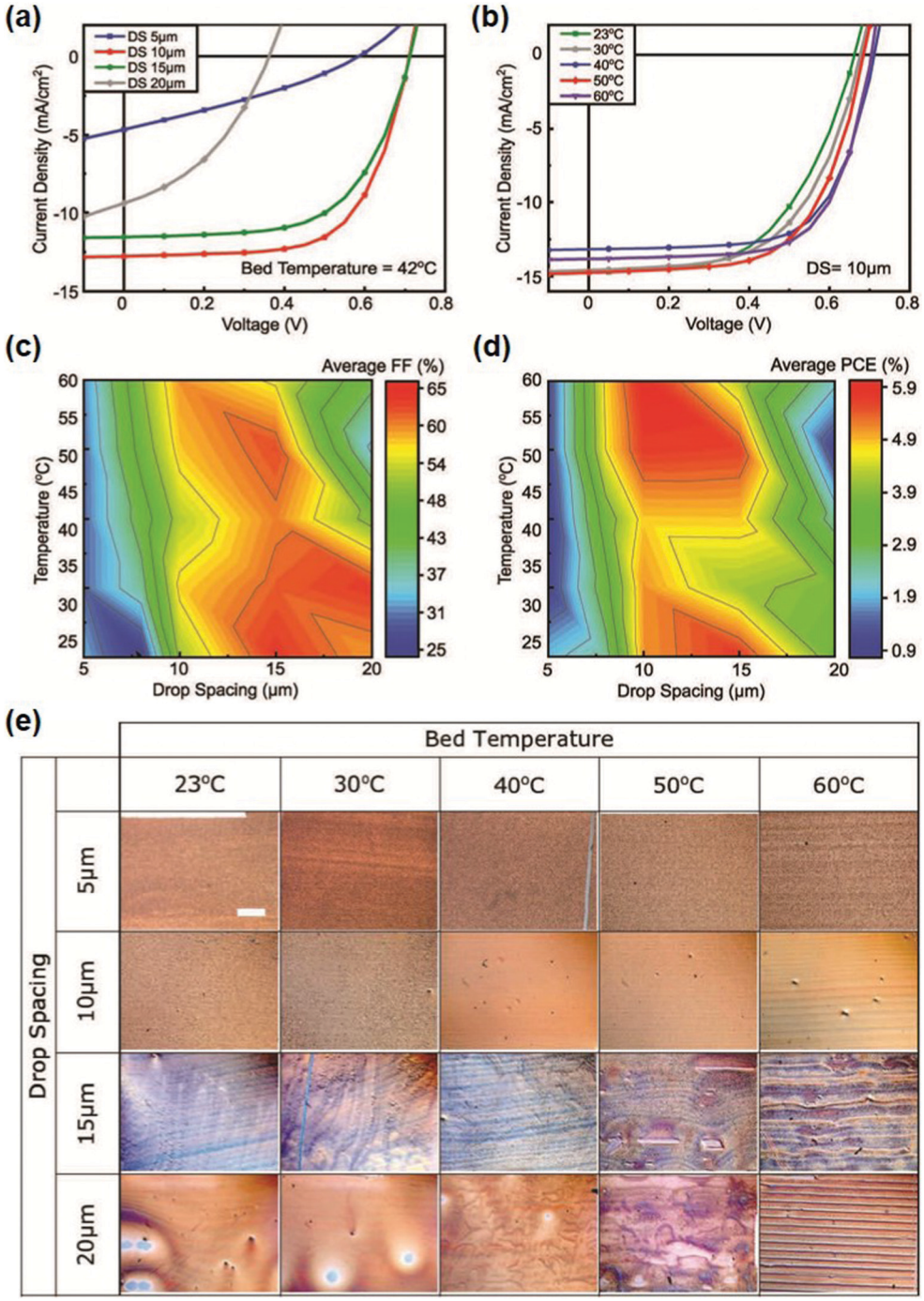

Fig. 16 (a) *J*–*V* curves of cells inkjet-printed at different drop spacing values at a constant bed temperature of 42 °C. (b) *J*–*V* curves of cells inkjet-printed with a fixed drop spacing of 10 μm and changing bed temperature. (c) and (d) Performance maps showing the average fill factor (FF) and PCEs of films inkjet-printed at varying drop spacing and bed temperature values. (e) Optical microscope images displaying the effects of drop spacing and bed temperature for deposition on the homogeneity and uniformity of P3HT:*o*-IDTBR films (scale bar = 500 μm). Adapted with permission.[124] Copyright 2019, Wiley-VCH Verlag GmbH & Co. KGaA.

printing, a composite ink of ZnO and polyethylenimine (PEI) was developed.[128] Modification of ZnO nanoparticles by PEI effectively improved the ink stability and mechanical properties. A PCE of 6% was obtained for the flexible device based on a PTB7-Th:$PC_{71}BM$ active layer with a thick R2R printed ZnO:PEI interfacial layer (~120 nm).

In addition to ZnO, some other metal oxides also exhibit good thickness tolerance. For example, Tan *et al.*[129] reported a chemically precipitated SnO_2 nanoparticle as the cathode interfacial layer, which exhibited excellent thickness tolerance. When the thickness of blade-coated SnO_2 layers is up to 530 nm, the PCE of PM6:Y6-based 4 mm^2 OSCs remained 12.08%,

just slightly lower than that for the 40 nm-SnO_2 counterpart (14.45%). For large-area OSCs (100 mm^2 area) with a blade-coated 100 nm-thick SnO_2 layer, the PCE reached 12.7%.

Some n-doped organic semiconductors based on perylene diimide and naphthalene diimide also exhibit good thickness tolerance. For example, Hou *et al.*[130] used (*N*,*N*-dimethylamino)-propyl naphthalene diimide (NDI-N) as a printable cathode interfacial layer. Based on the device structure of ITO/PEDOT:PSS/PM6:IT-4F/NDI-N/Ag, a large-area OSC device (1 cm^2) was fabricated with a blade-coated NDI-N layer. Compared with ZnO nanoparticle and PFN-Br interfacial layers, blade-coated NDI-N layers exhibited a smoother and more uniform surface, better wetting properties on the active layer surface and a greater thickness tolerance; a PCE of 13.2% was achieved.

Compared with the active layer and cathode interfacial layer, the anode interfacial layer generally exhibits poor thickness tolerance, which impedes the realization of large-area printed OSCs with high efficiency. A doping strategy is usually used to improve the charge transport properties and thickness tolerance of interfacial layers. An n-doped molybdenum oxide anode interfacial layer, which is an aqueous solution of ammonium heptamolybdate precursor with ethylene glycol, was reported by Hou *et al.*[131] With this ethylene glycol-based molybdenum oxide as the anode interfacial layer (*ca.* 10 nm), OSCs based on PB3T:IT-M exhibited PCEs of 12.1% (spin coating), 11.9% (wire-bar coating) and 11.5% (blade-coating). The device performance was insensitive to the anode interfacial layer thickness variation. When the thickness of the anode interfacial layer increased to 60 nm, the OSC still exhibited a PCE over 11%. In addition, 1 cm^2 area devices with a wire-bar coated anode interfacial layer also exhibited a high PCE of 10.1%. By adding vitamin C into ammonium molybdate tetrahydrate, another n-doped MoO_x (H:V-Mo) can be prepared.[132] Compared with pristine MoO_x, the conductivity of n-doped MoO_x was dramatically improved by four orders of magnitude, from 1.2×10^{-7} S m^{-1} to 1.1×10^{-3} S m^{-1}. By varying the thickness of the H:V-Mo anode interfacial layer from 10 to 150 nm, the V_{OC} and FF of the devices were almost the same. Based on the device structure of ITO/ZnO/PB3T2:IT-M/bladed H:V-Mo/Al, a PCE of 10.6% was achieved, slightly lower than that of spin-coated H:V-Mo based devices (11.1%).

Doped polyelectrolytes are another kind of anode interfacial layer material. For example, a p-type self-doped conjugated polyelectrolyte, PCP-3B, is a printable anode interfacial layer for large-area OSCs synthesized by Xu *et al.*[133] As a cyclopentadithiophene-based polymer, PCP-3B shows a high conductivity of 2.85×10^{-3} S m^{-1}, comparable to that of the traditional MoO_x interfacial material, a high work function of 5.01 eV, comparable to that of PEDOT:PSS, and good wetting properties on the ITO surface. Based on the PCP-3B anode interfacial layer, a 1 cm^2 PBDB-T:IT-M-based all blade-coated device achieved a PCE of 9.67%. PEDOT:PSS is the most common anode interfacial layer in conventional spin-coated OSCs. However, in inverted OSCs, particularly with a large area, the film formation of aqueous PEDOT:PSS on the hydrophobic active layer is a challenge. The mismatch in surface energy causes de-wetting and finally induces the formation of inhomogeneous layers. To solve this problem, surfactants are employed in aqueous PEDOT:PSS solution. Groen *et al.*[134] adopted a combination of alcohol, 1-pentanol and a fluorosurfactant (Capstone FS-3100) as the additive to effectively reduce the surface tension of aqueous PEDOT:PSS, which finally helped to form a homogeneous PEDOT:PSS film on the active layer. This transport layer exhibited good thickness tolerance, where the device performance was almost maintained with the thickness of the PEDOT:PSS layer varying from 50 nm to 400 nm.

4.3 Electrodes

For lab-scale OSCs, ITO is the most widely used transparent electrode. However, considering its brittleness and insufficient abundance, it is considered as a bottleneck for fab-scale device fabrication. Some researchers replaced ITO using carbon-based materials, conducting polymers, metal grids and metal nanowires.

Carbon-based materials mainly refer to graphene and carbon nanotubes (CNTs). Graphene and CNTs exhibit unique physical and chemical properties: high optical transparency, high electrical conductivity, good chemical and thermal stability and excellent mechanical flexibility, and are ideal candidates for transparent electrodes.[135] For example, Matsuo *et al.*[136] employed single-walled CNTs to fabricate metal-free semi-transparent OSCs. The single-walled CNT film was p-doped using two dopants: HNO_3 doped *via* sandwich transfer and MoO_3 doped *via* bridge transfer. Peng *et al.*[137] demonstrated a continuous R2R production of a transparent conductive flexible film with a structure of PET/ethylene vinyl acetate/silver nanowire/graphene. A large-area graphene film was grown on a Cu foil *via* a R2R chemical vapor deposition process. Then, this film was hot-laminated onto an Ag nanowire precoated PET film. Afterwards, the Cu foil was reused through a R2R electrochemical delamination process. This transparent electrode exhibited a low sheet resistance of 8 Ω sq^{-1} with a high transmittance of 94% at 550 nm. Ge *et al.*[138] reported a transparent electrode consisting of graphene, an Ag nanowire and a PH1000 composite. With this graphene/Ag nanowire/PH1000 hybrid electrode, OSCs based on PM6:Y6 exhibited a high PCE of 13.4%. The device retained 84.6% of its initial PCE after bending 1000 times (r = 2 mm), showing excellent mechanical flexibility.

The solution-processed transparent conducting polymer PEDOT:PSS has some advantages: high optical transparency in the visible light region, high work function (*ca.* 5.0 eV) and low cost, which is beneficial for flexible electrode fabrication. The cost of solution-processed PEDOT:PSS electrodes is less than 1% of that of ITO electrodes.[139,140] The conductivity of PEDOT:PSS is improved through doping or post-treatment strategies, while some pristine PEDOT:PSS solution (PEDOT:PSS 4083) exhibits low conductivity, less than 10^{-3} S cm^{-1}. Some solvents (*N*,*N*-dimethylformamide, dimethyl sulfoxide, ethylene glycol, tetrahydrofuran, *etc.*), surfactants and ionic liquids are used to improve conductivity. Inganäs *et al.*[141] firstly reported doping of glycerol into PEDOT:PSS solution. Kim *et al.*[142] reported that doping dimethyl sulfoxide into PEDOT:PSS solution (PH500) can improve the conductivity from 1 S cm^{-1} to $>$500 S cm^{-1}. The conductivity of PEDOT:PSS films can be improved to $>$2000 S cm^{-1} by doping strategies. Ge *et al.*[143] dropped PEDOT:PSS aqueous solution (PH1000) onto PET plastic substrates to

fabricate flexible electrodes. With dimethyl sulfoxide/methanesulfonic acid treated PEDOT:PSS electrodes, flexible OSCs based on PBDB-T:IT-M active layers displayed a PCE of 10.23%. The PEDOT:PSS layer discussed above can be used not only as the bottom electrode but also as the top electrode. Hou *et al.*[144] reported a spin-coated PEDOT:PSS layer as the top electrode; a PCE of 7.6% was realized in the flexible large-area (2.03 cm^2) OSCs with the architecture of Ag/TiO_x/PTB7-Th:ITIC/PEDOT:PSS.

Metal grids/meshes and metal nanowires are widely adopted as transparent electrodes owing to their inherent advantages, *e.g.* easy solution processing, high conductivity, and high transmittance in visible and NIR regions. For metal grids/meshes, post-treatments, *e.g.* thermal annealing, laser sintering and acid treatments, are widely employed to improve conductivity. For example, Lee *et al.*[145] reported that a post-annealing process of the Ag nanogrid at 170 °C can reduce the average sheet resistance from 250.3 to 15.2 Ω sq^{-1}. Blom *et al.*[146] used an effective photonic sintering process to fabricate printed metal grids in OSCs; the resistivity of Ag grids fabricated by a photonic sintering process for 5 s was similar to the resistivity of those fabricated by oven thermal sintering at 130 °C for 6 h. Silver nanowires (Ag NWs) have attracted great attention due to their excellent conductivity, high transparency and flexibility. They are widely used in hybrid electrode fabrication. For example, Wei *et al.*[147] employed Ag NWs as the bottom electrode, which was deposited on a flexible PET substrate by cross slot-die coating. Compared with ITO electrodes, the conducting PET/cross-coated Ag NW flexible film exhibited a transmittance of 94.9% to 70.8% in the visible range and a high conductivity. A large area (7 cm^2) flexible OSC based on PPDT2FBT:PCBM exhibited a PCE of 3.04%. Yu *et al.*[148] fabricated a transparent hybrid electrode: the inkjet-printed Ag grid was combined with Ag NWs. The printed Ag grid fills the gap between the Ag NWs and reduces the sheet resistance of the Ag NW film. The hybrid electrode exhibited a low sheet resistivity of 22.5 Ω sq^{-1} with a high transmittance of 89% at 550 nm, which is comparable to ITO electrodes. Li *et al.*[149] reported a PET/embedded Ag/Ag NWs/Al-doped ZnO composite flexible electrode. The hybrid electrode exhibited a low sheet resistance of 18 Ω sq^{-1} with an average transmittance of 84% in the range of 500–1000 nm; the flexible OSCs based on PM6:Y6 exhibited high PCEs of 15.21% (0.04 cm^2) and 12.28% (1 cm^2), respectively. Direct inkjet printing of a patterned, high-quality Ag NW network is relatively difficult. In order to avoid nozzle congestion, the ink concentration, printing parameters and post-treatment have to be carefully adjusted. For example, Coleman *et al.*[150] developed a well-defined Ag NW pattern by inkjet-printing an optimized isopropyl alcohol-diethylene glycol dispersion. The addition of diethylene glycol into a diluted isopropyl alcohol suspension enabled the ink to be printable without any satellite droplets.

5. Printed devices and modules

5.1 Large-area or flexible printed OSCs

In order to achieve a gradual transfer from small-scale to large-scale OSC fabrication, three stages are involved: (1) vacuum evaporation-assisted stage: the active and transport layers are processed with scalable technologies, such as slot-die coating and inkjet printing, while the top electrodes are still thermally vacuum-evaporated; (2) fully R2R-compatible stage: replacing vacuum evaporated electrodes with a solution-processed alternative, fully R2R-compatible devices or modules are fabricated; (3) ITO-free, R2R processing stage: replacing sputtered ITO front transparent electrodes with a solution-processed transparent electrode, each layer is R2R printed.

For the first stage, large-area devices and modules developed rapidly. Facchetti *et al.*[151] used *o*-xylene as the solvent to fabricate doctor-bladed modules based on TPD-3F:IT-4F, which exhibited a certified PCE of 10.4% for an area of 20.4 cm^2. In addition, the same module delivered a PCE of 22% under indoor lighting. Wei *et al.*[152] adopted a honeycomb PET/silver-grid as the electrode with slot-die coating. The PTB7-Th:COi8DFIC:$PC_{71}BM$ active layer was slot-die-coated at a high temperature (80 °C) with *o*-xylene as the processing solvent. They fabricated a flexible single-cell of 1 cm^2 with a high PCE of 12.16%. For modules with areas of 25 and 50 cm^2, PCEs of 10.09% and 9.05% were achieved, respectively. Furthermore, this flexible silver-grid OSC exhibited excellent mechanical bending performance. After 1000 bending cycles, the PCE remained at 94% (radius = 5 mm) and 99% (radius = 10 mm) of its initial value (Fig. 17). Zhou *et al.*[153] reported large-area flexible devices with PCEs of 13.1% and 12.6% with areas of 6 and 10 cm^2, respectively, and flexible modules with a PCE of 13.2% (54 cm^2) based on PET/Ag grid/Ag NW:PEI-Zn/PM6:Y6:$PC_{71}BM$/MoO_3/Ag. The PEI-Zn is beneficial for filling the Ag NW network void spaces, decreasing the surface roughness of the Ag NW film from 10.4 nm to 2.3 nm, and improving the thermal stability. The flexible OSCs almost retained their initial PCE values even after 1000 bending cycles (radius = 4 mm). Zan *et al.*[154] fabricated a 214 cm^2 OSC module based on PBDB-T:ITIC:$PC_{71}BM$, which yielded a PCE of 7.7%. By the blade coating method, a uniform active layer can be formed. This large-area module exhibited good stability, and the PCE was maintained at 86% after 140 days of storage at room temperature, 86% after 35 days of storage at 65 °C and 73% after 30 days of storage at 85 °C.

For the second stage, only a few studies on fully-printed, vacuum-free processed non-fullerene OSCs have been reported. The first work was published in 2013 by Zhan *et al.*[155] who reported a large-area inverted all-polymer solar cell by a R2R processing method. The active layer consisted of a PDI-based polymer, PDI-DTT, as the electron acceptor and a dithienosilole-based polymer, PSBTBT, as the electron donor. An inverted structure of ITO/ZnO nanoparticle/active layer/PEDOT:PSS/Ag was used. The ZnO layer, active layer and PEDOT:PSS layer were slot-die-coated, and an Ag back electrode was deposited using a R2R compatible flat-bed screen printing. A 4.2 cm^2 large-area module with a PCE of 0.204% was successfully fabricated. In 2018, Brabec *et al.*[156] designed a fully solution-processed R2R compatible module with the device structure of ITO/ZnO nanoparticle/P3HT:*o*-IDTBR/PEDOT:PSS/Ag NWs. All printed layers were processed using a home-made doctor blading coater. They fabricated a fully-printed small area device (0.104 cm^2) with Ag NWs as the top electrode. Furthermore, they upscaled a single

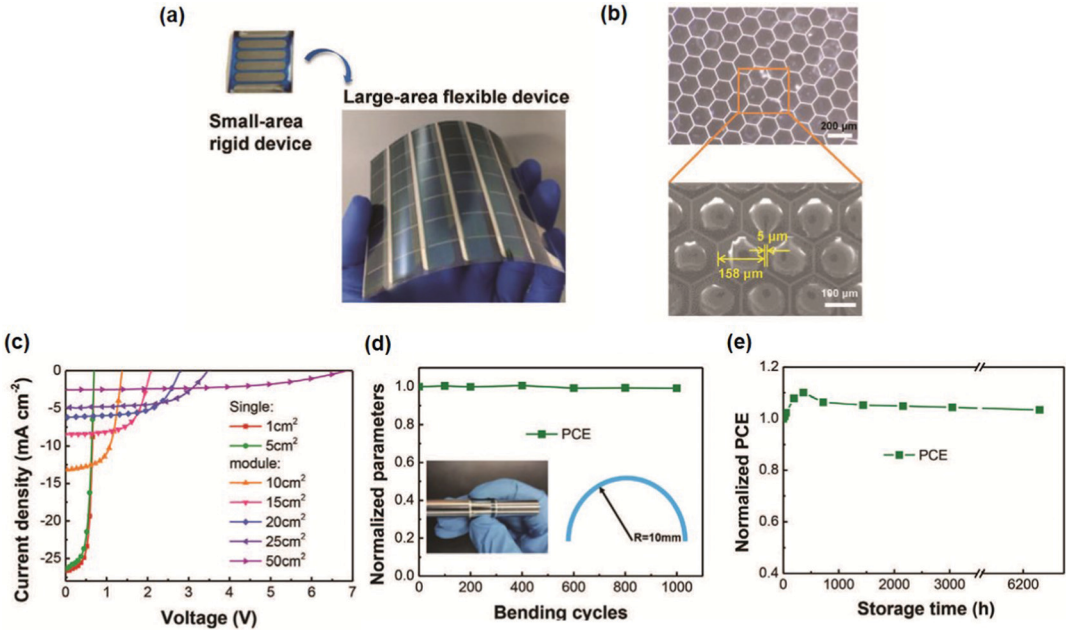

Fig. 17 (a) The small area rigid device and large-area flexible device. (b) Optical microscopy and SEM images of the PET/silver-grid substrate. (c) *J*–*V* curves of the PTB7-Th:COi8DFIC:$PC_{71}BM$ film coated by the slot-die method with different device areas. (d) Bending stability test. (e) Storage stability of devices in a nitrogen glove box. Adapted with permission.[152] Copyright 2020, Wiley-VCH Verlag GmbH & Co. KGaA.

cell to a module with a 59.5 cm^2 area. The module exhibited a PCE of 4.7%.

Replacing the bottom ITO electrode with solution-processed electrodes is the final stage. In 2014, Zhan *et al.*[157] fabricated a fully R2R processed fullerene-free OSC. The all-polymer solar cells with an inverted device structure of Ag/PEDOT:PSS/ZnO/PBDTTT-C-T:PDI-DTT/PEDOT:PSS/Ag exhibited an average PCE of 0.67% for 1 cm^2 devices. In the following year, they reported a fullerene-free large-area printed OSC based on the polymer donor PBDTTT-C-T and the non-fullerene small molecule acceptor DC-IDT2T. A PCE of 1.019% was achieved with a large device area (1 cm^2) on flexible substrates. The devices are ITO-free and fabricated under vacuum-free and ambient conditions. This fullerene-free device showed superior stability under continuous AM 1.5G illumination, maintaining more than 80% of their initial efficiency, compared with the fullerene-based device (50%).[158] In 2016, Zhan *et al.*[159] reported a fully-printed device based on PTB7-Th:IEIC as the active layer (Fig. 18). They employed two types of flexible device structures on a PET foil: (1) ITO-free, Ag/PEDOT:PSS/ZnO/PTB7-Th:IEIC/PEDOT:PSS/Ag, and (2) ITO, ITO/ZnO/PTB7-Th:IEIC/PEDOT:PSS/Ag. The ITO-free devices were fabricated using flexographic printing for the electrodes and slot-die coating for the other layers. For the ITO-free devices, an average PCE of 1.60% with a champion PCE of 1.79% was obtained for 1 cm^2 devices.

5.2 Green production

Green production methods, including green synthetic methods and green processing methods, are important for future large-scale OSC fabrication.[160,161] The widely used toxic halogenated solvents, *e.g.* chloroform, chlorobenzene and dichlorobenzene, are incompatible for large-scale industrial production. Adopting halogen-free solvents in fabrication of large-area OSC devices and modules is an emerging topic. Liu *et al.*[162] used 2-methyltetrahydrofuran as the solvent to regulate the morphology of all-polymer devices based on the PTzBI-Si:N2200 active layer. A high PCE of 10.15% was achieved with a 1 cm^2 device area. Huang *et al.*[163] reported sequentially blade-coated OSCs based on PM6:Y6. With *o*-xylene as the solvent, a PCE of 11.4% was obtained for large-area (1 cm^2) OSCs. Furthermore, Huang *et al.*[164] reported a large-area module (18 cm^2) based on PM6:DTY6 with a high efficiency of 14.4% when processed from *o*-xylene as the non-halogen solvent. The module retained 89% of the efficiency when the device area was scaled up from 0.04 cm^2 (PCE = 16.1%) to 18 cm^2. Lee *et al.*[165] fabricated a large-area OSC module (100 cm^2 of substrate size, 55.5 cm^2 of aperture size) with an encouraging PCE of 9.32% based on PTB7-Th:EH-IDTBR:T2-OEHRH as the active layer. The whole module was processed with toluene as the solvent under air conditions using a D-bar coating. This is one of the highest efficiencies for the NFA-based large-area OSC devices processed from green solvents.

5.3 Device encapsulation

The overall market feasibility of organic photovoltaics relies on not only high efficiency, fabrication scalability and environmental friendliness, but also long lifetime. Development of new barrier materials and encapsulation strategies to protect the sensitive active layer from moisture and oxygen ingress is essential for prolonging the lifespan of large-scale OSC devices and modules. Furthermore, barrier materials can block UV irradiation, improve thermal stability, and protect the device

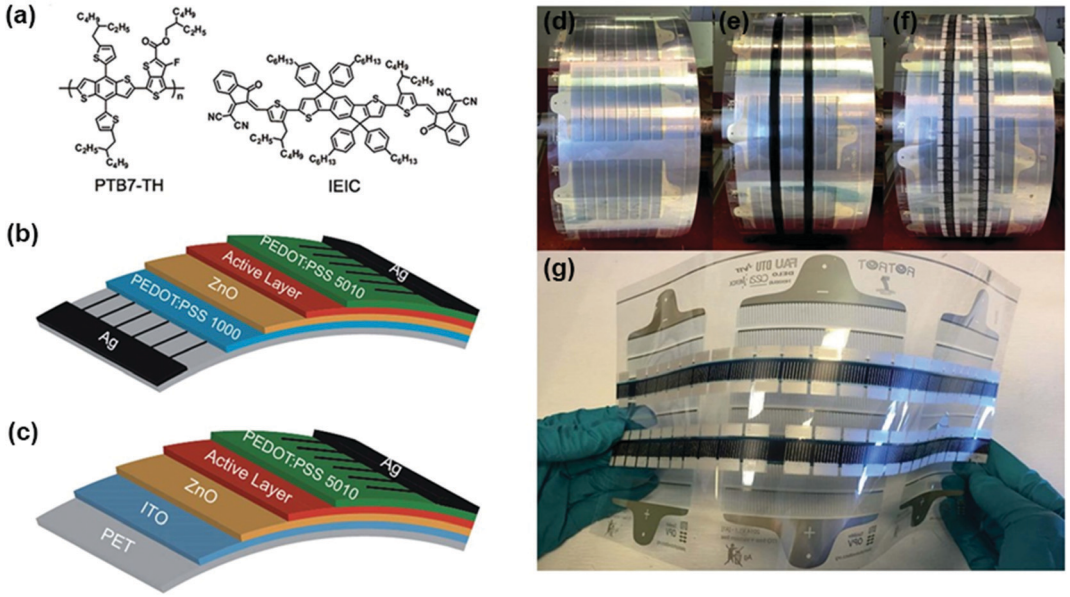

Fig. 18 (a) The molecular structures of PTB7-Th and IEIC. The structures of the OSCs based on (b) an ITO-free substrate and (c) a flexible ITO substrate. (d) PEDOT:PSS (PH1000) and ZnO coated PET flexible substrates with an Ag grid (ITO-free substrate). (e) Slot-die coating of the active layer of PTB7-Th:IEIC and PEDOT:PSS interfacial layers. (f) Flexographic printing of the top Ag electrode. (g) Long stripes of roll-coated FREA OSCs based on the ITO-free substrate. Adapted with permission.[159] Copyright 2016, The Royal Society of Chemistry.

from mechanical degradation. Flexible thin glass, flexible polymers, reactive polymer nanocomposites and single/multilayer organic and/or inorganic thin films are emerging flexible barrier materials in encapsulation.[166,167]

In the roll-to-roll fabrication process of printed OSC devices and modules, the final step is roll-to-roll encapsulation. Krebs *et al.*[168] summarized three effective R2R encapsulation lamination strategies, namely UV-curable epoxy resin, hot melting and pressure sensitive adhesives. In fact, no real R2R encapsulation has been performed on flexible non-fullerene-based OSC devices. Madsen *et al.*[169] adopted a combination of R2R vacuum deposition and sheet-to-sheet slot-die coating to fabricate an ITO-free, 7.14 cm^2 OSC module based on PET/Ag/ZnO/PBDB-T:ITIC/HTL solar/CPP PEDOT:PSS. The OSC module was encapsulated with two types of flexible barrier films, namely a commercial barrier film (3M Ultra Barrier Films 510) and a new barrier film based on a single 100 nm thick layer of zinc-tin-oxide deposited on a peelable-clean-surface film (Dupont Teijin Films). With the barrier film protection, a long stability under dark conditions over 1000 hours for the OSC module was achieved.

6. Summary and perspective

Large-area OSCs with high PCEs are highly desired for future applications. However, the photovoltaic performance of fab-scale devices still lags behind the lab-scale ones. Coating/printing technology, upscaling equipment and various device component processing strategies are key aspects for upscaling large-area OSCs.

Spin coating is the most widely used method in small-area device fabrication, but the high material waste and uncontrollable pattern are not suitable for large-area fabrication. Some large-area printing methods show great potential for upscaling devices, such as spray coating, inkjet printing, blade coating, rotary screen printing, flat-bed screen printing, knife-over-edge coating, slot-die coating, gravure printing and flexographic printing. Blade coating is widely used for active layer printing in fab-scale trials owing to its low cost and easy processing. Slot-die coating and inkjet printing are often used in shape-free devices because of their high resolution and high material utilization. As for metallic electrodes, screen printing and flexographic printing are more proper because these printing technologies are suitable for printing high viscosity inks. In a fully R2R process, various coating/printing technologies are required. By choosing a set of suitable operating parameters (ink velocity, ink volatility, processing parameters, *etc.*) in different coating/printing technologies, coffee ring, nozzle clogging and satellite droplet formation can be avoided and a high-efficiency R2R process can be carried out.

Lab-to-fab upscaling requires not only advanced fabrication technology, but also the development of equipment and the proper design of modules. At the lab stage, a desktop-based system is usually adopted to test new fabrication technologies. However, this non-integrated lab-scale equipment cannot be directly used in a R2R system. A roll-based system was developed from a single mini roll-coater to a fab-scale R2R system. A relatively complete R2R production line should be composed of a series of processing units, including an unwinding and in-feeding system unit, a printing and coating unit, a drying unit and a rewinding unit. Furthermore, testing and analysis units are also important for a production line to weed out bad products.

Apart from upscaling of fabrication technology and equipment, various device (or module) component processing strategies are

also important. Here, the device (or module) component includes the active layer, the interfacial layer and the electrodes. For the active layer, the film forming and drying behaviors are different by using different coating or printing methods in large-area devices. Meanwhile, in large-area printing, non-fullerene acceptors exhibit different packing and aggregation behaviors compared with fullerene acceptors. New strategies to construct high-performance non-fullerene-based large-area OSCs are highly desired. By solvent engineering (including cosolvents, additives, *etc.*) and other printing parameter engineering strategies (including adjusting ink temperature, substrate temperature, printing speed, *etc.*), ink properties and film formation can be controlled. For interfacial layers, thickness tolerant cathode/anode interfacial layer materials are desired. The low conductivity and poor wetting properties restrict thicker and smoother interfacial layer printing. Doping, post-treatment and more strategies can effectively fix the above-mentioned problems. For electrodes, replacing sputtered ITO bottom electrodes and thermally evaporated top electrodes is the future development direction. Electrodes with high transmittance in visible and NIR regions, low sheet resistance, and easy solution processing, including graphene, carbon nanotubes, PEDOT:PSS, Ag nanowires and Ag nanoparticles, developed rapidly.

The development from lab-scale to fab-scale R2R-processed OSCs involved three stages: (1) vacuum evaporation-assisted stage; (2) fully solution-processed, R2R-compatible stage; and (3) ITO-free, fully R2R stage. There are limited studies on fully-printed, vacuum-free processing of fullerene-free OSCs. For devices or modules with areas larger than 50 cm^2, even 100 cm^2, they mostly still stay in the vacuum evaporation-assisted stage and had not reached the fully R2R solution processing stage yet. Enlarging device or module areas, maintaining high PCE values and achieving fully R2R solution processing is the future development direction. For the upscaling of OSCs the following issues need to be addressed. Firstly, exploring thickness insensitive active layers and interfacial layers are essential. Non-fullerene acceptors, particularly FREAs, exhibit high exciton diffusion lengths and high electron mobilities, and have a great potential for fabricating thick-film active layers. Designing novel photoactive layer materials with higher mobility or adopting ternary blend strategies is beneficial for fabricating thick active layers. As for interfacial layers, apart from doping strategies, surface passivation can be used to effectively decrease the number of surface defects and improve charge transport properties and interfacial contact between the active layer and the interfacial layer, which may be effective for enhancing the thickness-tolerance of interfacial layers. Secondly, for lab-scale and fab-scale printing/coating technologies, the ink rheology and solvent volatilization behavior are different. A deeper understanding of film forming dynamic processes and physical mechanisms has been acquired. Analyzing physical mechanisms and adopting proper printing process parameters are required to produce homogeneous layers, including the active layer, interfacial layers and electrode layers. Thirdly, *in situ* morphology testing to weed out bad products is important, while *in situ* morphology measurements are assembled in lab-trials. The integration of high-speed measurements into a R2R production line is still a challenge. Except for GISAXS measurements, LBIC systems, photoluminescence, electroluminescence imaging and lock-in thermography are being developed to study defects. Fourthly, assembling single cells to a module with a high GFF is essential. Exploring high-resolution and low-cost laser patterning technology is a tendency for achieving a high GFF in large-area OSCs. By combining appropriate printing/coating methods, stable and effective fabrication equipment lines and effective device component processing strategies, high-performance large-area OSCs can be realized in the near future.

Conflicts of interest

The authors declare no conflicts of interest.

Acknowledgements

This work was supported by the National Natural Science Foundation of China (21734001 and 51761165023).

References

1 G. Li, R. Zhu and Y. Yang, *Nat. Photonics*, 2012, **6**, 153–161.
2 L. Lu, T. Zheng, Q. Wu, A. M. Schneider, D. Zhao and L. Yu, *Chem. Rev.*, 2015, **115**, 12666–12731.
3 D. Kearns and M. Calvin, *J. Chem. Phys.*, 1958, **29**, 950–951.
4 C. W. Tang, *Appl. Phys. Lett.*, 1986, **48**, 183–185.
5 M. Hiramoto, H. Fujiwara and M. Yokoyama, *Appl. Phys. Lett.*, 1991, **58**, 1062–1064.
6 G. Yu, J. Gao, J. C. Hummelen, F. Wudl and A. J. Heeger, *Science*, 1995, **270**, 1789–1791.
7 J. J. M. Halls, C. A. Walsh, N. C. Greenham, E. A. Marseglia, R. H. Friend, S. C. Moratti and A. B. Holmes, *Nature*, 1995, **376**, 498–500.
8 P. Cheng, G. Li, X. Zhan and Y. Yang, *Nat. Photonics*, 2018, **12**, 131–142.
9 M. C. Scharber, *Adv. Mater.*, 2016, **28**, 1994–2001.
10 Y. Lin, J. Wang, Z. Zhang, H. Bai, Y. Li, D. Zhu and X. Zhan, *Adv. Mater.*, 2015, **27**, 1170–1174.
11 Y. Lin, Q. He, F. Zhao, L. Huo, J. Mai, X. Lu, C.-J. Su, T. Li, J. Wang, J. Zhu, Y. Sun, C. Wang and X. Zhan, *J. Am. Chem. Soc.*, 2016, **138**, 2973–2976.
12 J. Wang and X. Zhan, *Acc. Chem. Res.*, 2021, **54**, 132–143.
13 C. Yan, S. Barlow, Z. Wang, H. Yan, A. K.-Y. Jen, S. R. Marder and X. Zhan, *Nat. Rev. Mater.*, 2018, **3**, 18003.
14 Y. Lin, F. Zhao, Q. He, L. Huo, Y. Wu, T. C. Parker, W. Ma, Y. Sun, C. Wang, D. Zhu, A. J. Heeger, S. R. Marder and X. Zhan, *J. Am. Chem. Soc.*, 2016, **138**, 4955–4961.
15 S. Dai, F. Zhao, Q. Zhang, T.-K. Lau, T. Li, K. Liu, Q. Ling, C. Wang, X. Lu, W. You and X. Zhan, *J. Am. Chem. Soc.*, 2017, **139**, 1336–1343.
16 F. Zhao, S. Dai, Y. Wu, Q. Zhang, J. Wang, J. Li, Q. Ling, Z. Wei, W. Ma, W. You, C. Wang and X. Zhan, *Adv. Mater.*, 2017, **29**, 1700144.
17 S. Dai, T. Li, W. Wang, Y. Xiao, T.-K. Lau, Z. Li, K. Liu, X. Lu and X. Zhan, *Adv. Mater.*, 2018, **30**, 1706571.

18 J. Wang, J. Zhang, Y. Xiao, T. Xiao, R. Zhu, C. Yan, Y. Fu, G. Lu, X. Lu, S. R. Marder and X. Zhan, *J. Am. Chem. Soc.*, 2018, **140**, 9140–9147.
19 B. Jia, J. Wang, Y. Wu, M. Zhang, Y. Jiang, Z. Tang, T. P. Russell and X. Zhan, *J. Am. Chem. Soc.*, 2019, **141**, 19023–19031.
20 T. Li, Y. Wu, J. Zhou, M. Li, J. Wu, Q. Hu, B. Jia, X. Pan, M. Zhang, Z. Tang, Z. Xie, T. P. Russell and X. Zhan, *J. Am. Chem. Soc.*, 2020, **142**, 20124–20133.
21 J. Yuan, Y. Zhang, L. Zhou, G. Zhang, H.-L. Yip, T.-K. Lau, X. Lu, C. Zhu, H. Peng, P. A. Johnson, M. Leclerc, Y. Cao, J. Ulanski, Y. Li and Y. Zou, *Joule*, 2019, **3**, 1140–1151.
22 F. Liu, L. Zhou, W. Liu, Z. Zhou, Q. Yue, W. Zheng, R. Sun, W. Liu, S. Xu, H. Fan, L. Feng, Y. Yi, W. Zhang and X. Zhu, *Adv. Mater.*, 2021, **33**, 2100830.
23 L. Zhan, S. Li, X. Xia, Y. Li, X. Lu, L. Zuo, M. Shi and H. Chen, *Adv. Mater.*, 2021, **33**, 2007231.
24 C. Li, J. Zhou, J. Song, J. Xu, H. Zhang, X. Zhang, J. Guo, L. Zhu, D. Wei, G. Han, J. Min, Y. Zhang, Z. Xie, Y. Yi, H. Yan, F. Gao, F. Liu and Y. Sun, *Nat. Energy*, 2021, **6**, 605–613.
25 P. Cheng, J. Wang, X. Zhan and Y. Yang, *Adv. Energy Mater.*, 2020, **10**, 2000746.
26 L. Meng, Y. Zhang, X. Wan, C. Li, X. Zhang, Y. Wang, X. Ke, Z. Xiao, L. Ding, R. Xia, H.-L. Yip, Y. Cao and Y. Chen, *Science*, 2018, **361**, 1094–1098.
27 P. Cheng, Y. Liu, S.-Y. Chang, T. Li, P. Sun, R. Wang, H.-W. Cheng, T. Huang, L. Meng, S. Nuryyeva, C. Zhu, K.-H. Wei, B. Sun, X. Zhan and Y. Yang, *Joule*, 2019, **3**, 432–442.
28 P. Cheng, H.-C. Wang, R. Zheng, Y. Zhu, S. Dai, Z. Li, C.-H. Chen, Y. Zhao, R. Wang, D. Meng, C. Zhu, K.-H. Wei, X. Zhan and Y. Yang, *Adv. Mater.*, 2020, **32**, 2002315.
29 W. Wang, C. Yan, T.-K. Lau, J. Wang, K. Liu, Y. Fan, X. Lu and X. Zhan, *Adv. Mater.*, 2017, **29**, 1701308.
30 C. Sun, R. Xia, H. Shi, H. Yao, X. Liu, J. Hou, F. Huang, H.-L. Yip and Y. Cao, *Joule*, 2018, **2**, 1816–1826.
31 S. Dai and X. Zhan, *Adv. Energy Mater.*, 2018, **8**, 1800002.
32 P. Cheng, H.-C. Wang, Y. Zhu, R. Zheng, T. Li, C. H. Chen, T. Huang, Y. Zhao, R. Wang, D. Meng, Y. Li, C. Zhu, K.-H. Wei, X. Zhan and Y. Yang, *Adv. Mater.*, 2020, **32**, 2003891.
33 J. Zhang, G. Xu, F. Tao, G. Zeng, M. Zhang, Y. Yang, Y. Li and Y. Li, *Adv. Mater.*, 2019, **31**, 1807159.
34 Q. Liu, L. G. Gerling, F. B. Texca, J. Toudert, T. Li, X. Zhan and J. Martorell, *Adv. Energy Mater.*, 2020, **10**, 1904196.
35 V. V. Brus, J. Lee, B. R. Luginbuhl, S.-J. Ko, G. C. Bazan and T.-Q. Nguyen, *Adv. Mater.*, 2019, **31**, 1900904.
36 C. Ballif, L.-E. Perrt-Aebi, S. Lufkin and E. Rey, *Nat. Energy*, 2018, **3**, 438–442.
37 E. Ravishankar, R. E. Booth, C. Saravitz, H. Sederoff, H. W. Ade and B. T. O'Connor, *Joule*, 2020, **4**, 490–506.
38 S. Chandrabose, K. Chen, A. J. Barker, J. J. Sutton, S. K. K. Prasad, J. Zhu, J. Zhou, K. C. Gordon, Z. Xie, X. Zhan and J. M. Hodgkiss, *J. Am. Chem. Soc.*, 2019, **141**, 6922–6929.
39 S. Dai, J. Zhou, S. Chandrabose, Y. Shi, G. Han, K. Chen, J. Xin, K. Liu, Z. Chen, Z. Xie, W. Ma, Y. Yi, L. Jiang, J. M. Hodgkiss and X. Zhan, *Adv. Mater.*, 2020, **32**, 2000645.
40 J. Zhou, X. Wen, N. Tang, X. Zhou, C. Wang, N. Zheng, L. Liu and Z. Xie, *J. Phys. Chem. Lett.*, 2020, **11**, 7908–7913.
41 J. Huang, J. Lee, J. Vollbrecht, V. V. Brus, A. L. Dixon, D. X. Cao, Z. Zhu, Z. Du, H. Wang, K. Cho, G. C. Bazan and T.-Q. Nguyen, *Adv. Mater.*, 2020, **32**, 1906027.
42 F. C. Krebs, S. A. Gevorgyan and J. Alstrup, *J. Mater. Chem.*, 2009, **19**, 5442–5451.
43 R. R. Søndergaard, M. Hösel and F. C. Krebs, *J. Polym. Sci., Part B: Polym. Phys.*, 2013, **51**, 16–34.
44 Y. W. Han, S. J. Jeon, H. S. Lee, H. Park, K. S. Kim, H.-W. Lee and D. K. Moon, *Adv. Energy Mater.*, 2019, **9**, 1902065.
45 F. C. Krebs, *Sol. Energy Mater. Sol. Cells*, 2009, **93**, 394–412.
46 X. Peng, J. Yuan, S. Shen, M. Gao, A. S. R. Chesman, H. Yin, J. Cheng, Q. Zhang and D. Angmo, *Adv. Funct. Mater.*, 2017, **27**, 1703704.
47 A. S. Gertsen, M. F. Castro, R. R. Søndergaard and J. W. Andreasen, *Flexible Printed Electron.*, 2020, **5**, 014004.
48 G. Wang, M. A. Adil, J. Zhang and Z. Wei, *Adv. Mater.*, 2019, **31**, 1805089.
49 G. Bernardo, T. Lopes, D. G. Lidzey and A. Mendes, *Adv. Energy Mater.*, 2021, **11**, 2100342.
50 L. Lucera, P. Kubis, F. W. Fecher, C. Bronnbauer, M. Turbiez, K. Forberich, T. Ameri, H.-J. Egelhaaf and C. J. Brabec, *Energy Technol.*, 2015, **3**, 373–384.
51 G. Hashmi, K. Miettunen, T. Peltola, J. Halme, I. Asghar, K. Aitola, M. Toivola and P. Lund, *Renewable Sustainable Energy Rev.*, 2011, **15**, 3717–3732.
52 R. Søndergaard, M. Hösel, D. Angmo, T. T. Larsen-Olsen and F. C. Krebs, *Mater. Today*, 2012, **15**, 36–49.
53 H. Youn, H. J. Park and L. J. Guo, *Small*, 2015, **11**, 2228–2246.
54 R. Abbel, Y. Galagan and P. Groen, *Adv. Eng. Mater.*, 2018, **20**, 1701190.
55 M. D. M. Faure and B. H. Lessard, *J. Mater. Chem. C*, 2021, **9**, 14–40.
56 M. Kuang, L. Wang and Y. Song, *Adv. Mater.*, 2014, **26**, 6950–6958.
57 D. Tian, Y. Song and L. Jiang, *Chem. Soc. Rev.*, 2013, **42**, 5184–5209.
58 K. X. Steirer, M. O. Reese, B. L. Rupert, N. Kopidakis, D. C. Olson, R. T. Collins and D. S. Ginley, *Sol. Energy Mater. Sol. Cells*, 2009, **93**, 447–453.
59 S. Arumugam, Y. Li, S. Senthilarasu, R. Torah, A. L. Kanibolotsky, A. R. Inigo, P. J. Skabara and S. P. Beeby, *J. Mater. Chem. A*, 2016, **4**, 5561–5568.
60 A. Reale, L. L. Notte, L. Salamandra, G. Polino, G. Susanna, T. M. Brown, F. Brunetti and A. D. Carlo, *Energy Technol.*, 2015, **3**, 385–406.
61 M. Pilch and C. A. Erdman, *Int. J. Multiphase Flow*, 1987, **13**, 741–757.
62 S. Nešić and J. Vodnik, *Chem. Eng. Sci.*, 1991, **46**, 527–537.
63 R. Rioboo, C. Tropea and M. Marengo, *Atomization Sprays*, 2001, **11**, 155–165.
64 C. N. Hoth, S. A. Choulis, P. Schilinsky and C. J. Brabec, *Adv. Mater.*, 2007, **19**, 3973–3978.
65 M. Singh, H. M. Haverinen, P. Dhagat and G. E. Jabbour, *Adv. Mater.*, 2010, **22**, 673–685.

66 O. A. Basaran, H. Gao and P. P. Bhat, *Annu. Rev. Fluid Mech.*, 2013, **45**, 85–113.
67 S. K. Karunakaran, G. M. Arumugam, W. Yang, S. Ge, S. N. Khan, X. Lin and G. Yang, *J. Mater. Chem. A*, 2019, **7**, 13873–13902.
68 B. Derby and N. Reis, *MRS Bull.*, 2003, **28**, 815–818.
69 Y. Aleeva and B. Pignataro, *J. Mater. Chem. C*, 2014, **2**, 6436–6453.
70 J. Willmann, D. Stocker and E. Dörsam, *Org. Electron.*, 2014, **15**, 1631–1640.
71 Y.-M. Chang, C.-Y. Liao, C.-C. Lee, S.-Y. Lin, N.-W. Teng and P. H.-S. Tan, *Sol. Energy Mater. Sol. Cells*, 2019, **202**, 110064.
72 I. Burgués-Ceballos, M. Stella, P. Lacharmoise and E. Martínez-Ferrero, *J. Mater. Chem. A*, 2014, **2**, 17711–17722.
73 Q. Wu, J. Guo, R. Sun, J. Guo, S. Jia, Y. Li, J. Wang and J. Min, *Nano Energy*, 2019, **61**, 559–566.
74 J. Lee, A. Kim, S. M. Cho and H. Chae, *Korean J. Chem. Eng.*, 2012, **29**, 337–340.
75 J. Yang, D. Vak, N. Clark, J. Subbiah, W. W. H. Wong, D. J. Jones, S. E. Watkins and G. Wilson, *Sol. Energy Mater. Sol. Cells*, 2013, **109**, 47–55.
76 D. Vak, H. Weerasinghe, J. Ramamurthy, J. Subbiah, M. Brown and D. J. Jones, *Sol. Energy Mater. Sol. Cells*, 2016, **149**, 154–161.
77 C. Kapnopoulos, E. D. Mekeridis, L. Tzounis, C. Polyzoidis, A. Zachariadis, S. Tsimikli, C. Gravalidis, A. Laskarakis, N. Vouroutzis and S. Logothetidis, *Sol. Energy Mater. Sol. Cells*, 2016, **144**, 724–731.
78 F. Bonaccorso, A. Bartolotta, J. N. Coleman and C. Backes, *Adv. Mater.*, 2016, **28**, 6136–6166.
79 T. Morita, V. Singh, S. Nagamatsu, S. Oku, W. Takashima and K. Kaneto, *Appl. Phys. Express*, 2009, **2**, 111502.
80 J. Noh, S. Jeong and J.-Y. Lee, *Nat. Commun.*, 2016, **7**, 12374.
81 A. Kumar, S. Ratan, D. K. Jarwal, A. K. Mishra, C. Kumar, A. P. Singh, B. Mukherjee and S. Jit, *Mater. Res. Express*, 2019, **6**, 115514.
82 R. Wang, L. Lüer, S. Langner, T. Heumueller, K. Forberich, H. Zhang, J. Hauch, N. Li and C. J. Brabec, *ChemSusChem*, 2021, **14**, 3590–3598.
83 R. Runser, S. E. Root, D. E. Ober, K. Choudhary, A. X. Chen, C. Dhong, A. D. Urbina and D. J. Lipomi, *Chem. Mater.*, 2019, **31**, 9078–9086.
84 S. Hong, J. Lee, H. Kang and K. Lee, *Sol. Energy Mater. Sol. Cells*, 2013, **112**, 27–35.
85 F. C. Krebs, M. Jørgensen, K. Norrman, O. Hagemann, J. Alstrup, T. Nielson, J. Fyenbo, K. Larsen and J. Kristensen, *Sol. Energy Mater. Sol. Cells*, 2009, **93**, 422–441.
86 P. Kopola, T. Aernouts, S. Guillerez, H. Jin, M. Tuomikoski, A. Maaninen and J. Hast, *Sol. Energy Mater. Sol. Cells*, 2010, **94**, 1673–1680.
87 M. M. Voigt, R. C. I. Mackenzie, S. P. King, C. P. Yau, P. Atienzar, J. Dane, P. E. Keivanidis, D. D. C. Bradley and J. Nelson, *Sol. Energy Mater. Sol. Cells*, 2011, **95**, 731–734.
88 M. M. Voigt, R. C. I. Mackenzie, S. P. King, C. P. Yau, P. Atienzar, J. Dane, P. E. Keivanidis, I. Zadrazil, D. D. C. Bradley and J. Nelson, *Sol. Energy Mater. Sol. Cells*, 2012, **105**, 77–85.
89 H. F. Dam and F. C. Krebs, *Sol. Energy Mater. Sol. Cells*, 2012, **97**, 191–196.
90 J. E. Carlé, T. R. Andersen, M. Helgesen, E. Bundgaard, M. Jørgensen and F. C. Krebs, *Sol. Energy Mater. Sol. Cells*, 2013, **108**, 126–128.
91 J. E. Carlé, M. Helgesen, N. K. Zawacka, M. V. Madsen, E. Bundgaard and F. C. Krebs, *J. Polym. Sci., Part B: Polym. Phys.*, 2014, **52**, 893–899.
92 M. Helgesen, J. E. Carlé and F. C. Krebs, *Adv. Energy Mater.*, 2013, **3**, 1664–1669.
93 M. J. Griffith, N. A. Cooling, B. Vaughan, K. M. O'Donnell, M. F. Al-Mudhaffer, A. Al-Ahmad, M. Noori, F. Almyahi, W. J. Belcher and P. C. Dastoor, *Energy Technol.*, 2015, **3**, 428–436.
94 T. R. Andersen, H. F. Dam, M. Hösel, M. Helgesen, J. E. Carlé, T. T. Larsen-Olsen, S. A. Gevorgyan, J. W. Andreasen, J. Adams, N. Li, F. Machui, G. D. Spyropoulos, T. Ameri, N. e. Lemaître, M. Legros, A. Scheel, D. Gaiser, K. Kreul, S. Berny, O. R. Lozman, S. Nordman, M. Välimäki, M. Vilkman, R. R. Søndergaard, M. Jørgensen, C. J. Brabec and F. C. Krebs, *Energy Environ. Sci.*, 2014, **7**, 2925–2933.
95 L. H. Rossander, N. K. Zawacka, H. F. Dam, F. C. Krebs and J. W. Andreasen, *AIP Adv.*, 2014, **4**, 087105.
96 H. F. Dam, T. R. Andersen, E. B. L. Pedersen, K. T. S. Thydén, M. Helgesen, J. E. Carlé, P. S. Jørgensen, J. Reinhardt, R. R. Søndergaard, M. Jørgensen, E. Bundgaard, F. C. Krebs and J. W. Andreasen, *Adv. Energy Mater.*, 2015, **5**, 1400736.
97 F. C. Krebs, M. Hösel, M. Corazza, B. Roth, M. V. Madsen, S. A. Gevorgyan, R. R. Søndergaard, D. Karg and M. Jørgensen, *Energy Technol.*, 2013, **1**, 378–381.
98 R. Rösch, F. C. Krebs, D. M. Tanenbaum and H. Hoppe, *Sol. Energy Mater. Sol. Cells*, 2012, **97**, 176–180.
99 A. Karl, A. Osvet, A. Vetter, P. Maisch, N. Li, H.-J. Egelhaaf and C. J. Brabec, *Prog. Photovoltaics*, 2019, **27**, 460–468.
100 F. C. Krebs, R. Søndergaard and M. Jørgensen, *Sol. Energy Mater. Sol. Cells*, 2011, **95**, 1348–1353.
101 E. Pascual-San-José, G. Sadoughi, L. Lucera, M. Stella, E. Martínez-Ferrero, G. E. Morse, M. Campoy-Quiles and I. Burgués-Ceballos, *J. Mater. Chem. A*, 2020, **8**, 9882–9895.
102 R. Tipnis, J. Bernkopt, S. Jia, J. Krieg, S. Li, M. Storch and D. Laird, *Sol. Energy Mater. Sol. Cells*, 2009, **93**, 442–446.
103 S. Röttinger, B. Schwarz, S. Schäfer, R. Gauch, B. Zimmermann and U. Würfel, *Sol. Energy Mater. Sol. Cells*, 2016, **154**, 35–41.
104 P. Kubis, N. Li, T. Stubhan, F. Machui, G. J. Matt, M. M. Voigt and C. J. Brabec, *Prog. Photovoltaics*, 2015, **23**, 238–246.
105 L. Lucera, F. Machui, P. Kubis, H. D. Schmidt, J. Adams, S. Strohm, T. Ahmad, K. Forberich, H.-J. Egelhaaf and C. J. Brabec, *Energy Environ. Sci.*, 2016, **9**, 89–94.
106 A. Distler, C. J. Brabec and H.-J. Egelhaaf, *Prog. Photovoltaics*, 2021, **29**, 24–31.
107 P. Maisch, K. C. Tam, P. Schilinsky, H.-J. Egelhaaf and C. J. Brabec, *Sol. RRL*, 2018, **2**, 1800005.
108 S. Hong, H. Kang, G. Kim, S. Lee, S. Kim, J.-H. Lee, J. Lee, M. Yi, J. Kim, H. Back, J.-R. Kim and K. Lee, *Nat. Commun.*, 2016, **7**, 10279.

109 H. Kim, S. Lee, D. Han and S. Yoo, *Sol. Energy Mater. Sol. Cells*, 2014, **120**, 561–565.
110 T. M. Eggenhuisen, Y. Galagan, A. F. K. V. Biezemans, T. M. W. L. Slaats, W. P. Voorthuijzen, S. Kommeren, S. Shanmugam, J. P. Teunissen, A. Hadipour, W. J. H. Verhees, S. C. Veenstra, M. J. J. Coenen, J. Gilot, R. Andriessen and W. A. Groen, *J. Mater. Chem. A*, 2015, **3**, 7255–7262.
111 S. Berny, N. Blouin, A. Distler, H.-J. Egelhaaf, M. Krompiec, A. Lohr, O. R. Lozman, G. E. Morse, L. Nanson, A. Pron, T. Sauermann, N. Seidler, S. Tierney, P. Tiwana, M. Wagner and H. Wilson, *Adv. Sci.*, 2016, **3**, 1500342.
112 M. Välimäki, E. Jansson, P. Korhonen, A. Peltoniemi and S. Rousu, *Nanoscale Res. Lett.*, 2017, **12**, 117.
113 V. Bergeron, D. Bonn, J. Y. Martin and L. Vovelle, *Nature*, 2000, **405**, 772–775.
114 D. Jang, D. Kim and J. Moon, *Langmuir*, 2009, **25**, 2629–2635.
115 K. Chang, Y. Li, G. Du, M. Zhong, P. Yang, Y. Zhu, F. He, B. Mi, X. Zhao and W. Deng, *ACS Appl. Mater. Interfaces*, 2020, **12**, 27405–27415.
116 W. Zhao, S. Zhang, Y. Zhang, S. Li, X. Liu, C. He, Z. Zheng and J. Hou, *Adv. Mater.*, 2018, **30**, 1704837.
117 L. Zhang, H. Zhao, J. Yuan, B. Lin, Z. Xing, X. Meng, L. Ke, X. Hu, W. Ma and Y. Yuan, *Org. Electron.*, 2020, **83**, 105771.
118 K. S. Wienhold, V. Körstgens, S. Grott, X. Jiang, M. Schwartzkopf, S. V. Roth and P. Müller-Buschbaum, *ACS Appl. Mater. Interfaces*, 2019, **11**, 42313–42321.
119 L. Zhang, B. Lin, B. Hu, X. Xu and W. Ma, *Adv. Mater.*, 2018, **30**, 1800343.
120 L. Ye, Y. Xiong, Q. Zhang, S. Li, C. Wang, Z. Jiang, J. Hou, W. You and H. Ade, *Adv. Mater.*, 2018, **30**, 1870054.
121 S.-I. Na, Y.-H. Seo, Y.-C. Nah, S.-S. Kim, H. Heo, J.-E. Kim, N. Rolston, R. H. Dauskardt, M. Gao, Y. Lee and D. Vak, *Adv. Funct. Mater.*, 2019, **29**, 1805825.
122 H. Zhao, H. B. Naveed, B. Lin, X. Zhou, J. Yuan, K. Zhou, H. Wu, R. Guo, M. A. Scheel, A. Chumakov, S. V. Roth, Z. Tang, P. Müller-Buschbaum and W. Ma, *Adv. Mater.*, 2020, **32**, 2002302.
123 L. Zhang, H. Zhao, B. Lin, J. Yuan, X. Xu, J. Wu, K. Zhou, X. Guo, M. Zhang and W. Ma, *J. Mater. Chem. A*, 2019, **7**, 22265–22273.
124 D. Corzo, K. Almasabi, E. Bihar, S. Macphee, D. Rosas-Villalva, N. Gasparini, S. Inal and D. Baran, *Adv. Mater. Technol.*, 2019, **4**, 1900040.
125 X. Meng, L. Zhang, Y. Xie, X. Hu, Z. Xing, Z. Huang, C. Liu, L. Tan, W. Zhou, Y. Sun, W. Ma and Y. Chen, *Adv. Mater.*, 2019, **31**, 1903649.
126 G. Ji, W. Zhao, J. Wei, L. Yan, Y. Han, Q. Luo, S. Yang, J. Hou and C.-Q. Ma, *J. Mater. Chem. A*, 2019, **7**, 212–220.
127 J. Liu, J. Wu, S. Shao, Y. Deng, B. Meng, Z. Xie, Y. Geng, L. Wang and F. Zhang, *ACS Appl. Mater. Interfaces*, 2014, **6**, 8237–8245.
128 J. Wei, C. Zhang, G. Ji, Y. Han, I. Ismail, H. Li, Q. Luo, J. Yang and C.-Q. Ma, *Sol. Energy*, 2019, **193**, 102–110.
129 Y. Bai, C. Zhao, S. Zhang, S. Zhang, R. Yu, J. Hou, Z. a. Tan and Y. Li, *Sci. China: Chem.*, 2020, **63**, 957–965.
130 Q. Kang, L. Ye, B. Xu, C. An, S. J. Stuard, S. Zhang, H. Yao, H. Ade and J. Hou, *Joule*, 2019, **3**, 227–239.
131 Q. Kang, B. Yang, Y. Xu, B. Xu and J. Hou, *Adv. Mater.*, 2018, **30**, 1801718.
132 B. Yang, Y. Chen, Y. Cui, D. Liu, B. Xu and J. Hou, *Adv. Energy Mater.*, 2018, **8**, 1800698.
133 Q. Kang, Q. Liao, Y. Xu, L. Xu, Y. Zu, S. Li, B. Xu and J. Hou, *ACS Appl. Mater. Interfaces*, 2019, **11**, 20205–20213.
134 S. Kommeren, M. J. J. Coenen, T. M. Eggenhuisen, T. W. L. Slaats, H. Gorter and P. Groen, *Org. Electron.*, 2018, **61**, 282–288.
135 M. F. L. De Volder, S. H. Tawfick, R. H. Baughman and A. J. Hart, *Science*, 2013, **339**, 535–539.
136 I. I. Jeon, C. Delacou, A. Kaskela, E. I. Kauppinen, S. Maruyama and Y. Matsuo, *Sci. Rep.*, 2016, **6**, 31348.
137 B. Deng, P.-C. Hsu, G. Chen, B. N. Chandrashekar, L. Liao, Z. Ayitimuda, J. Wu, Y. Guo, L. Lin, Y. Zhou, M. Aisijiang, Q. Xie, Y. Cui, Z. Liu and H. Peng, *Nano Lett.*, 2015, **15**, 4206–4213.
138 W. Zhang, W. Song, J. Huang, L. Huang, T. Yan, J. Ge, R. Peng and Z. Ge, *J. Mater. Chem. A*, 2019, **7**, 22021–22028.
139 C. J. M. Emmott, A. Urbina and J. Nelson, *Sol. Energy Mater. Sol. Cells*, 2012, **97**, 14–21.
140 Y. Zhang, S.-W. Ng, X. Lu and Z. Zheng, *Chem. Rev.*, 2020, **120**, 2049–2122.
141 T. Granlund, T. Nyberg, L. S. Roman, M. Svensson and O. Inganäs, *Adv. Mater.*, 2000, **12**, 269–273.
142 S.-I. Na, S.-S. Kim, J. Jo and D.-Y. Kim, *Adv. Mater.*, 2008, **20**, 4061–4067.
143 H. Cui, W. Song, B. Fanady, R. Peng, J. Zhang, J. Huang and Z. Ge, *Sci. China: Chem.*, 2019, **62**, 500–505.
144 Y. Lin, Y. Jin, S. Dong, W. Zheng, J. Yang, A. Liu, F. Liu, Y. Jiang, T. P. Russell, F. Zhang, F. Huang and L. Hou, *Adv. Energy Mater.*, 2018, **8**, 1701942.
145 J. Kang, C.-G. Park, S.-H. Lee, C. Cho, D.-G. Choi and J.-Y. Lee, *Nanoscale*, 2016, **8**, 11217–11223.
146 Y. Galagan, E. W. C. Coenen, R. Abbel, T. J. van Lammeren, S. Sabik, M. Barink, E. R. Meinders, R. Andriessen and P. W. M. Blom, *Org. Electron.*, 2013, **14**, 38–46.
147 Y.-F. Zhao, W.-J. Zou, H. Li, K. Lu, W. Yan and Z.-X. Wei, *Chin. J. Polym. Sci.*, 2017, **35**, 261–268.
148 T. Ye, L. Jun, L. Kun, W. Hu, C. Ping, D. Ya-Hui, C. Zheng, L. Yun-Fei, W. Hao-Ran and D. Yu, *Org. Electron.*, 2017, **41**, 179–185.
149 X. Chen, G. Xu, G. Zeng, H. Gu, H. Chen, H. Xu, H. Yao, Y. Li, J. Hou and Y. Li, *Adv. Mater.*, 2020, **32**, 1908478.
150 D. J. Finn, M. Lotya and J. N. Coleman, *ACS Appl. Mater. Interfaces*, 2015, **7**, 9254–9261.
151 C.-Y. Liao, Y. Chen, C.-C. Lee, G. Wang, N.-W. Teng, C.-H. Lee, W.-L. Li, Y.-K. Chen, C.-H. Li, H.-L. Ho, P. H.-S. Tan, B. Wang, Y.-C. Huang, R. M. Young, M. R. Wasielewski, T. J. Marks, Y.-M. Chang and A. Facchetti, *Joule*, 2020, **4**, 189–206.
152 G. Wang, J. Zhang, C. Yang, Y. Wang, Y. Xing, M. A. Adil, Y. Yang, L. Tian, M. Su, W. Shang, K. Lu, Z. Shuai and Z. Wei, *Adv. Mater.*, 2020, **32**, 2005153.

153 F. Qin, L. Sun, H. Chen, Y. Liu, X. Lu, W. Wang, T. Liu, X. Dong, P. Jiang, Y. Jiang, L. Wang and Y. Zhou, *Adv. Mater.*, 2021, **33**, 2103017.
154 K.-M. Huang, C.-M. Lin, S.-H. Chen, S.-H. Chen, C.-S. Li, C.-H. Hu, Y. Zhang, H.-F. Meng, C.-Y. Chang, Y.-C. Chao, H.-W. Zan, L. Huo and P. Yu, *Sol. RRL*, 2019, **3**, 1900071.
155 Y. Liu, T. T. Larsen-Olsen, X. Zhao, B. Andreasen, R. R. Søndergaard, M. Helgesen, K. Norrman, M. Jørgensen, F. C. Krebs and X. Zhan, *Sol. Energy Mater. Sol. Cells*, 2013, **112**, 157–162.
156 S. Strohm, F. Machui, S. Langner, P. Kubis, N. Gasparini, M. Salvador, I. McCulloch, H.-J. Egelhaaf and C. J. Brabec, *Energy Environ. Sci.*, 2018, **11**, 2225–2234.
157 P. Cheng, Y. Lin, N. K. Zawacka, T. R. Andersen, W. Liu, E. Bundgaard, M. Jørgensen, H. Chen, F. C. Krebs and X. Zhan, *J. Mater. Chem. A*, 2014, **2**, 19542–19549.
158 P. Cheng, H. Bai, N. K. Zawacka, T. R. Andersen, W. Liu, E. Bundgaard, M. Jørgensen, H. Chen, F. C. Krebs and X. Zhan, *Adv. Sci.*, 2015, **2**, 1500096.
159 K. Liu, T. T. Larsen-Olsen, Y. Lin, M. Beliatis, E. Bundgaard, M. Jørgensen, F. C. Krebs and X. Zhan, *J. Mater. Chem. A*, 2016, **4**, 1044–1051.
160 Y. Huang and C. K. Luscombe, *Chem. Rec.*, 2019, **19**, 1039–1049.
161 Z. Du, M. Mainville, J. Vollbrecht, A. L. Dixon, N. Schopp, M. Schrock, Z. Peng, J. Huang, S. Chae, H. Ade, M. Leclerc, G. N. M. Reddy and T.-Q. Nguyen, *Sol. RRL*, 2021, **5**, 2100213.
162 L. Zhu, W. Zhong, C. Qiu, B. Lyu, Z. Zhou, M. Zhang, J. Song, J. Xu, J. Wang, J. Ali, W. Feng, Z. Shi, X. Gu, L. Ying, Y. Zhang and F. Liu, *Adv. Mater.*, 2019, **31**, 1902899.
163 S. Dong, K. Zhang, B. Xie, J. Xiao, H.-L. Yip, H. Yan, F. Huang and Y. Cao, *Adv. Energy Mater.*, 2019, **9**, 1802832.
164 S. Dong, T. Jia, K. Zhang, J. Jing and F. Huang, *Joule*, 2020, **4**, 2004–2016.
165 T. Lee, S. Oh, S. Rasool, C. E. Song, D. Kim, S. K. Lee, W. S. Shin and E. Lim, *J. Mater. Chem. A*, 2020, **8**, 10318–10330.
166 L. J. Sutherland, H. C. Weerasinghe and G. P. Simon, *Adv. Energy Mater.*, 2021, **11**, 2101383.
167 I. A. Channa, A. Distler, M. Zaiser, C. J. Brabec and H.-J. Egelhaaf, *Adv. Energy Mater.*, 2019, **9**, 1900598.
168 M. Hösel, R. R. Sønderggard, M. Jørgensen and F. C. Krebs, *Adv. Eng. Mater.*, 2013, **15**, 1068–1075.
169 E. Destouesse, M. Top, J. Lamminaho, H.-G. Rubahn, J. Fahlteich and M. Madsen, *Flexible Printed Electron.*, 2019, **4**, 045004.